

## RESEARCH ARTICLES

## MOLECULAR MAGNETISM

# Reaching the magnetic anisotropy limit of a 3d metal atom

Ileana G. Rau,<sup>1\*</sup> Susanne Baumann,<sup>1,2\*</sup> Stefano Rusponi,<sup>3</sup> Fabio Donati,<sup>3</sup> Sebastian Stepanow,<sup>4</sup> Luca Gragnaniello,<sup>3</sup> Jan Dreiser,<sup>3,5</sup> Cinthia Piamonteze,<sup>5</sup> Frithjof Nolting,<sup>5</sup> Shruba Gangopadhyay,<sup>1</sup> Oliver R. Albertini,<sup>1,6</sup> Roger M. Macfarlane,<sup>1</sup> Christopher P. Lutz,<sup>1</sup> Barbara A. Jones,<sup>1</sup> Pietro Gambardella,<sup>4,†</sup> Andreas J. Heinrich,<sup>1,†</sup> Harald Brune<sup>3,†</sup>

Designing systems with large magnetic anisotropy is critical to realize nanoscopic magnets. Thus far, the magnetic anisotropy energy per atom in single-molecule magnets and ferromagnetic films remains typically one to two orders of magnitude below the theoretical limit imposed by the atomic spin-orbit interaction. We realized the maximum magnetic anisotropy for a 3d transition metal atom by coordinating a single Co atom to the O site of an MgO(100) surface. Scanning tunneling spectroscopy reveals a record-high zero-field splitting of 58 millielectron volts as well as slow relaxation of the Co atom's magnetization. This striking behavior originates from the dominating axial ligand field at the O adsorption site, which leads to out-of-plane uniaxial anisotropy while preserving the gas-phase orbital moment of Co, as observed with x-ray magnetic dichroism.

**M**agnetic anisotropy (MA) provides directionality and stability to magnetization. Strategies to scale up the MA of ferromagnetic 3d metals have relied on introducing heavy elements within or next to the ferromagnet in order to enhance the spin-orbit coupling energy. Rare-earth transition-metal alloys, such as TbCoFe (1), and binary multilayers, such as Co/Pt and Co/Pd (2), are used as magnetic recording materials because of their large perpendicular MA (3). Recent experiments, however, have shown that Co and Fe thin films deposited on metallic oxides such as AlO<sub>x</sub> and MgO present MA energies on the order of 1 meV/atom (4, 5), which is similar to that of Co/Pt interfaces but driven by the electronic hybridization between the metal 3d and O 2p orbitals (6, 7). Perpendicular magnetic tunnel junctions, including CoFeB/MgO layers, are being intensively investigated for nonvolatile MRAM (magnetic random access memory) applications (5, 8, 9), in which the lateral dimensions of a magnetic bit approach 20 nm (10).

A fundamental constraint to the downscaling of magnetic devices is the total amount of

MA energy that can be induced in the storage layer, which limits its thermal stability factor and influences the rate of magnetization switching (11). As the dimensions of a magnetic bit shrink to the atomic scale, quantum-mechanical excitation and relaxation effects, which greatly affect the magnetization, can come into play. We explore the limit of how much MA can be stored in an atom and for how long it can retain a given spin state in a

model system of a single Co atom bound to an MgO layer. We show that this “bit” achieves the maximum possible MA energy for a 3d metal. This MA limit is ~60 meV, set by the atomic spin-orbit coupling strength times the unquenched orbital angular momentum. We measured spin relaxation times on the order of 200 μs at 0.6 K and show that the rate-limiting relaxation step for a Co atom is determined by the mixing of excited spin states into the ground state induced by nonaxial ligand field components.

## Magnetic Anisotropy in Quantum Systems

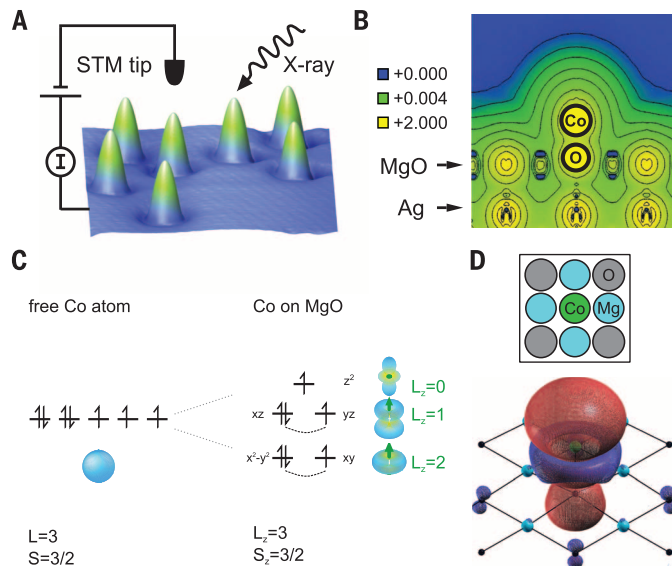
The microscopic origin of MA is the combined effect of the anisotropy in the atom's orbital angular momentum (**L**), together with the interaction between **L** and the atom's spin angular momentum (**S**). This interaction is given by  $H_{\text{SOC}} = \lambda \mathbf{L} \cdot \mathbf{S}$ , where  $\lambda$  is the atomic spin-orbit coupling parameter. In solids and molecules, **L** tends to align along specific symmetry directions, set by the spatial dependence of the ligand field. The strength of the MA is defined here by the so-called zero-field splitting (ZFS) (12), which is the energy difference between the electronic ground state and the first excited state that has its spin pointing in a different direction with respect to the ground state, in the absence of an external field. For spin-flip transitions that leave **L** unchanged, the ZFS is thus proportional to  $\lambda L$ , where  $\lambda$  is ~-22 meV for Co (13). However, in most magnetic compounds the orbital moment magnitude *L* is either quenched or strongly diminished by ligand field (14) and hybridization (15) effects, leading to MA energies on the order of 0.01 meV/atom in bulk magnets and up to ~1 meV/atom in thin films (16) and nanostructures (17). Achieving large ZFS

**Fig. 1. Co on MgO**

**films. (A)** Constant current STM image of seven Co atoms on 1 ML of MgO on Ag(100) at  $T = 1.2$  K (10 pA, 50 mV, 7.5 nm × 7.5 nm). Shown are schematic diagrams of STM (left) and XAS (right). **(B)** DFT-calculated structure and valence electron charge density of one Co atom atop an O atom in 1 ML MgO on Ag(100). Charge density color scale is in atomic units.

**(C)** Schematic model of the orbital occupancy of Co in a free atom

(left), in its <sup>4</sup>F term ( $L = 3$ ,  $S = 3/2$ ), and Co on the MgO surface (right). The orbital moment is preserved along the easy-axis of the Co in this cylindrical ligand field ( $L_z = 3$ ,  $S_z = 3/2$ ). **(D)** Top view of ball model of the atomic structure (top) and DFT calculation of the Co atom spin density of the valence electrons (bottom). Oblique view shows contours of constant positive (red) and negative (blue) spin polarization.



<sup>1</sup>IBM Almaden Research Center, 650 Harry Road, San Jose, CA 95120, USA. <sup>2</sup>Department of Physics, University of Basel, Klingelbergstrasse 82, CH-4056 Basel, Switzerland. <sup>3</sup>Institute of Condensed Matter Physics, Ecole Polytechnique Fédérale de Lausanne (EPFL), Station 3, CH-1015 Lausanne, Switzerland. <sup>4</sup>Department of Materials, Eidgenössische Technische Hochschule (ETH) Zürich, Höggerberggring 64, CH-8093 Zürich, Switzerland. <sup>5</sup>Swiss Light Source, Paul Scherrer Institute, CH-5232 Villigen PSI, Switzerland. <sup>6</sup>Department of Physics, Georgetown University, 3700 O Street NW, Washington, DC 20057, USA.

\*These authors contributed equally to this work. †Corresponding author. E-mail: andreash@us.ibm.com (A.J.H.); pietro.gambardella@mat.ethz.ch (P.G.); harald.brune@epfl.ch (H.B.)

in transition metals requires somehow breaking the spatial symmetry of the atomic wavefunctions without quenching the orbital magnetization. The most promising strategy to preserve the large  $L$  of a free atom and induce uniaxial anisotropy is to use low-coordination geometries, as shown for atoms deposited on the threefold coordinated sites of a (111) surface (18, 19) and molecular complexes and crystals with two-coordinate metal species (20–24). This strategy, if specific conditions are met, can be brought to its limit by coordinating one magnetic atom to a single substrate atom.

We achieved this extreme by using cobalt, which has  $L = 3$ , the highest in the transition metal series, and a thin film of MgO as a substrate with a onefold (“atop”) coordinated site for adsorbed transition metal atoms (25). Co atoms were deposited on a single MgO layer grown on Ag(100) (26–28). They appear as protrusions that are  $0.15 \pm 0.02$  nm high when imaged with scanning tunneling microscopy (STM) (Fig. 1A). The preferred binding site, determined with

density functional theory (DFT), is on top of oxygen (Fig. 1B) (26) with four Mg atoms as neighbors, resulting in  $C_{4v}$  symmetry. Despite the presence of these four Mg atoms, the spin density of the valence electrons of the Co is rotationally symmetric around  $z$  (effectively  $C_{\infty v}$ ) (Fig. 1D). This axial coordination can preserve the orbital moment of the free atom along the vertical axis but quench it in-plane (Fig. 1C). The DFT density of states of the Co  $d$ -levels (Fig. 2) shows that the interaction with the Mg atoms is weak and the Co  $d_{xz^2-y^2}$ ,  $d_{xy}$  orbitals remain largely degenerate. The dominant bond is between the out-of-plane  $d$  orbitals of Co and  $p$  orbitals of O, resulting in an uniaxial ligand field along  $z$ . DFT calculations further indicate that the Co atom is charge-neutral and has spin magnitude  $S = 1.39 \pm 0.05$ .

### Measurement of the ZFS with STM

We used inelastic electron tunneling spectroscopy (IETS) (19, 29–32) to probe the quantum spin

states of the Co atoms (26). In such a measurement, electrons tunneling from the STM tip may transfer energy and angular momentum to a magnetic atom and induce spin-flip excitations above a threshold voltage. The IETS spectrum of a Co atom on 1 monolayer (ML) MgO at 0.6 K is shown in Fig. 3A. We observed a sudden stepwise increase in conductance at  $\pm 57.7$  mV, symmetric around zero bias, as expected for an inelastic excitation. The  $dI/dV$  step is magnetic in origin and splits into two in an applied magnetic field (Fig. 3, B and C). For ease of discussion, we begin by approximating the magnetic state of the Co atom as an  $S = 3/2$  system with uniaxial anisotropy (later in the paper, we will include the effects of configuration mixing and the presence of large orbital moment). We assign these excitations to transitions between the ground ( $S_z = \pm 3/2$ , labeled as states 0 and 1 in Fig. 3D) and excited states ( $S_z = \pm 1/2$ , states 2 and 3). At zero field, the states 0 and 1, as well as 2 and 3, are degenerate and yield identical excitation voltages ( $V_{02} = V_{13}$ ). The two steps shift in accord with Zeeman energies, with the  $0 \rightarrow 2$  step shifting up and the  $1 \rightarrow 3$  shifting down in energy with increasing magnetic field, to yield a well-resolved splitting of  $1.8 \pm 0.2$  meV at 6 T.

The IETS measurements reveal a remarkable ZFS of 57.7 meV between ground and excited states. The ZFS is much larger than the typical values of several millielectron volts reported before for single atoms on surfaces (19, 30–33), which indicates an exceptionally high MA for Co on MgO. Moreover, the presence of the  $V_{13}$  step, in addition to the  $V_{02}$  step, at finite magnetic field is surprising because at low temperature ( $k_B T \ll eV_{01}$ , where  $k_B$  is the Boltzmann constant and  $T$  is temperature) and low applied voltage ( $V_{\text{bias}} < V_{02}$ ) one would expect only state 0 (the ground state) to be occupied for an appreciable fraction of the time. The observation of the  $1 \rightarrow 3$  transition for Co on MgO is an indication that the excited state 1 has a lifetime above 1 ns (the mean tunneling time between electrons at the measured currents).

### Electronic Structure Probed with X-ray Absorption Spectroscopy

To understand the large energy and time scales revealed by the IETS measurements, we performed x-ray absorption spectroscopy (XAS) of isolated Co atoms deposited on 2 to 4 MLs of MgO on Ag(100). By measuring the excitation cross-section for  $2p$  to  $3d$  transitions,  $L$ -edge x-ray absorption spectra provide a probe of the bonding and the magnetic properties of transition metal ions (34) that is highly complementary to IETS. Spectra acquired at the  $L_{3}$  Co edge with circularly polarized light are shown in Fig. 4A (26). The XAS lineshape differs from that of Co atoms adsorbed on metal substrates (18, 35) as well as from typical CoO phases (36), showing that the bonding of Co is specific to the MgO surface. The x-ray magnetic circular dichroism (XMCD) intensity measured at normal incidence is larger than at grazing incidence (Fig. 4B),

**Fig. 2. DFT spin-resolved partial density of states of the Co, O, and Mg levels.** The figure shows the large ligand field splitting induced by O ligation for the out-of-plane orbitals and also shows the degeneracy between the Co ( $d_{xz}, d_{yz}$ ) and ( $d_{xy}, d_{x^2-y^2}$ ) orbitals.

Large overlap between the Co  $d_{z^2}$  and O  $p_z$  as well as  $d_{xz}, d_{yz}$  and  $p_x, p_y$  orbitals indicates hybridization between Co and O, whereas no Co-Mg overlap is visible.

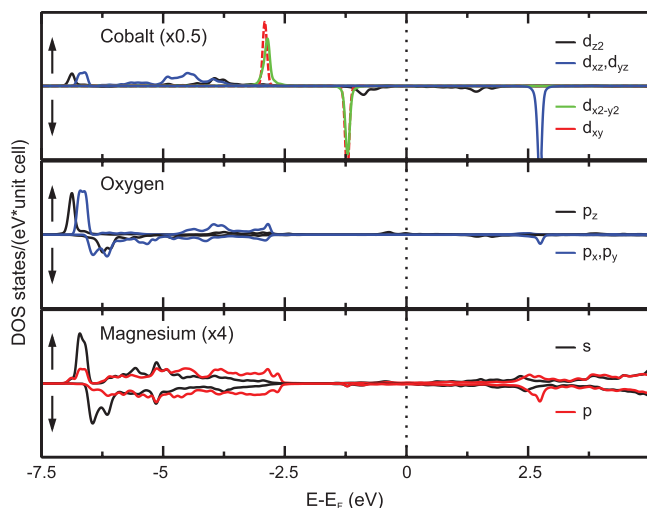
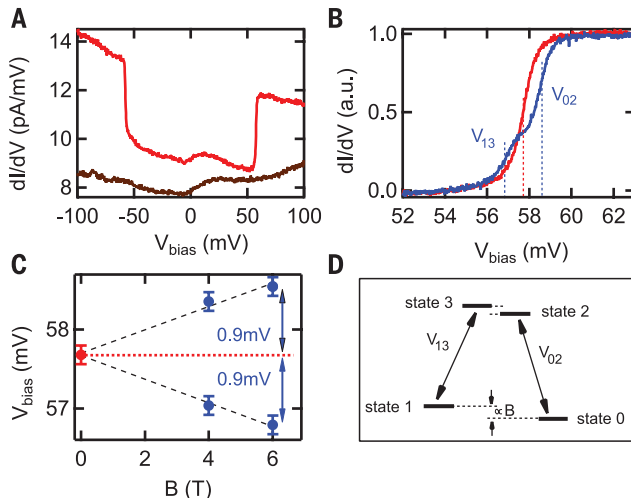


**Fig. 3. Magnetic excitations measured in STM at  $T = 0.6$  K.**

(A) Differential conductance spectrum ( $dI/dV$ ). The tip is positioned above a Co atom on 1 ML MgO on Ag(100) (red) and bare MgO (brown). (B) Expanded view of the steps near 58 mV for 0 T (red) and 6 T (blue) (tip height setpoint 5 nA, 100 mV). (C) The step position as a function of magnetic field, showing the field-induced splitting. Only one step is resolvable at 0 T (red point). Dashed lines are linear fits to the data points. (D) Schematic energy level diagram. The states are labeled in order of increasing energy from 0 to 3. The arrows  $V_{02}$  and  $V_{13}$  indicate the transitions measured in IETS.



which implies that the Co magnetic moment has an out-of-plane easy axis. The XMCD spectra reveal a large orbital-to-effective spin moment ratio, in the range of 0.9 to 1.2, which indicates that  $L$  is very large on this surface. A discussion of the XMCD sum rule analysis (37, 38) and technical challenges related to x-ray-induced desorption on thin insulating films (39) is reported in (26).

To determine the electronic ground state and the structure of the lowest lying magnetic states, we simulated the x-ray experimental results using multiplet ligand field theory (34). The multiplet calculations include charge transfer ( $\sigma$ -donation) via the  $d_{z^2}$  orbital and take into account the mixing between  $d^7$  and  $d^8l$  configurations, where  $l$  describes a ligand hole on the O site. As shown in Fig. 4, A and B, there is excellent agreement between the simulated and experimental XAS and XMCD. The resulting  $d$ -shell occupancy is 7.44 electrons, which is in good agreement with the DFT results [7.27 electrons in a Löwdin analysis (26, 40)]. The evolution of the calculated Co states as a function of ligand field splitting and spin-orbit interaction is shown in Fig. 4D [the complete energy diagram is provided in fig. S3 (26)]. The lowest energy level (Fig. 4D, left edge) is an octuplet (blue) with  $L_z = \pm 3 \otimes S_z = \pm 1.25$ ,  $S_z = \pm 0.42$ , where the spin moment is slightly less than the free atom value of  $S = 3/2$  because of mixing of the ground state

$^4F$  and  $^3F$  terms of the  $d^7$  and  $d^8$  configurations, respectively.

### Origin of the ZFS

The electronic states of Co after including all interactions—namely, ligand field, spin-orbit coupling, and external magnetic field—are shown on the right side of Fig. 4D. What is most unusual about the resulting spin doublet ground state is that it is composed of a mixture of states dominated by  $L_z = \pm 3$  and thus has an orbital moment near the free atom limit. Unlike previous reports, such a large  $L$  for a surface-adsorbed transition metal atom was observed here because the ligand field is essentially uniaxial [it does not lift the degeneracy between the ( $d_{xz}$ ,  $d_{yz}$ ) or between the ( $d_{x^2-y^2}$ ,  $d_{xy}$ ) orbitals], and both  $d^7$  and  $d^8$  configurations have the same orbital multiplicity so that configuration mixing—which takes place here, as it does on most substrates—does not reduce the magnitude of  $L$ .

The substantial orbital contribution can also be seen in the magnetization measured by XMCD as a function of applied field, which indicates a local moment of  $\sim 6\mu_B$  per atom (Fig. 4C) (where  $\mu_B$  is the Bohr magneton). This result is in agreement with the magnetization  $\mu_z = \langle L_z \rangle + \langle 2S_z \rangle$  calculated by using the wave functions and energy levels obtained from the multiplet simulations (Fig. 4C, solid black line). Both experimental

and theoretical curves saturate very fast, as expected for strong MA. At low magnetic fields, the measured values remain above the calculated values (Fig. 4C, inset), which could be the result of slow relaxation effects or induced magnetic moment contributions from the substrate atoms.

The multiplet energy diagram in Fig. 4D, derived from the model fit to the XAS data, provides a detailed interpretation of the IETS spectra. The calculated energy separation between the ground-state spin doublet (states 0 and 1) and the first excited spin doublet (states 2 and 3) at zero field is 55 meV, which closely matches the energy of the conductance step ( $V_{02} = V_{13} = 57.7$  mV) measured with IETS (26). This level of agreement between XAS and IETS is remarkable considering that these are independent experiments that take place at radically different energy scales (hundreds of electron volts for the x-ray measurements as compared with millielectron volts for IETS).

The multiplet results establish that the separation of the first two spin doublets at 0 T is the ZFS seen in IETS spectra and explain its magnitude. The key is the nearly unquenched orbital moment of the lowest energy levels, which allows the  $S_z = \pm 3/2$  states to be split maximally from the  $S_z = \pm 1/2$  states by the spin-orbit interaction. In this case, the ZFS is equal to  $\lambda L \Delta S_z$ , which for

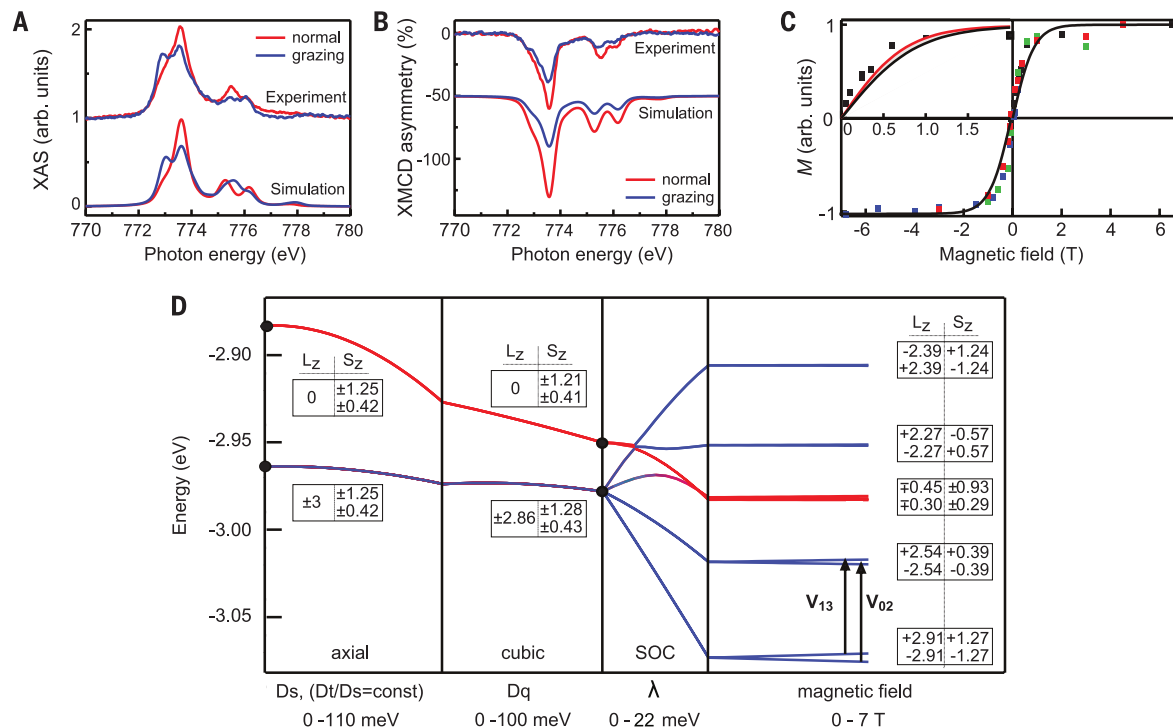


**Fig. 4. XMCD measurements and multiplet calculations.** (A) Experimental and simulated x-ray absorption spectra of Co/MgO/Ag(100) at normal ( $\theta = 0^\circ$ ) and grazing ( $\theta = 60^\circ$ ) incidence recorded over the  $L_3$  Co edge at  $T = 3.5$  K and  $B = 6.8$  T. The Co coverage is 0.03 ML. The spectra are the sum of positive and negative circular polarization, ( $I^+ + I^-$ ). (B) XMCD spectra ( $I^+ - I^-$ ). The XMCD intensity is given as percentage of the total absorption signal shown in (A). (C) Out-of-plane magnetization versus field at 3.5 K measured by XMCD after saturating the sample at 6.8 T (black, red, and green squares)

and  $-6.8$  T (blue) at each point. Different colors refer to different samples. The solid line represents the expectation value of  $\langle L_z \rangle + \langle 2S_z \rangle \approx 6\mu_B$  at 3.5 K. The inset (top left quadrant) compares fits between 3 (red curve) and 3.5 K (black). (D) Lowest energy levels with the multiplet calculations as a function of ligand field, spin-orbit coupling, and applied magnetic field. The color code of the energy levels highlights the different orbital symmetry of the states: blue for  $E$  and red for  $B_2$ . The two transitions seen in IETS are indicated by arrows.

Co (with  $L = 3$  and  $\Delta S_z = 1$ ) gives  $\lambda L \approx 60$  meV, reaching up to the full magnitude of the spin-orbit coupling energy intrinsic to a Co atom. This value is much higher than usually observed for transition metal systems, in which  $L$  arises as a perturbative effect because of spin-orbit coupling, and the ZFS has a second-order dependence on  $\lambda^2$  (41, 42).

### Spin Lifetime Measurements

The ZFS defines the energy for the lowest-order process required to surmount the barrier that separates 0 and 1, the states with large and opposite magnetic moments. Our experiments are at low temperature ( $k_B T \ll$  ZFS), which effectively suppresses thermal excitations of the magnetic moment over the MA energy barrier. These conditions offer the possibility to probe in detail nonthermal magnetization reversal mechanisms that become important when a magnet is scaled to atomic dimensions. In the case of magnetic atoms placed near electrodes (here, the Ag substrate and STM tip), spin relaxation can occur through  $\Delta S_z = \pm 1$  transitions induced by electrons from these electrodes that scatter off the magnetic atom and either tunnel across the junction or return to the original electrode (43). These scattering processes result in quantum tunneling of the magnetization (44, 45). These mechanisms are extremely sensitive to the local environment, such as the electronic density of states of the substrate and distortions of the ligand field surrounding the magnetic adatoms (45).

We now focus on measurements of the spin lifetime as a probe of the nonthermal decay mechanisms. The relaxation time  $T_1$  of excited spin states can be measured with spin-polarized STM with a pump-probe scheme (33). The current in a spin-polarized tunnel junction sensitively depends on the relative alignment of tip and sample spins (46). Thus, the tunnel current with the atom in the ground state is generally different from the current in an excited state. Sufficiently large pump pulses put the atom into excited spin

states, from which it eventually decays back to the ground state. This decay was monitored with a probe pulse. Such a pump-probe measurement is shown in Fig. 5A with an exponentially changing current, yielding a lifetime  $T_1 = 232 \pm 17 \mu\text{s}$  at 1 T. To determine which state is giving the long lifetime signals observed here, we measured the amplitude of the pump-probe signal as a function of pump voltage (Fig. 5, B and C), which shows an onset of the signal at  $59 \pm 2$  meV (Fig. 5B) and another sharp onset at  $1.9 \pm 0.1$  meV (Fig. 5C). The first threshold is in good agreement with  $V_{02}$  and indicates when state 1 can be reached via state 2. The 1.9-meV threshold corresponds to the direct excitation  $0 \rightarrow 1$ , which is in agreement with  $V_{01} = 2(L_z + 2S_z)\mu_B B$  calculated from the multiplet model at 3 T, demonstrating that we are measuring the lifetime of state 1. This Zeeman splitting yields a total magnetic moment of  $5.5 \pm 0.3\mu_B$ , which matches the magnetic moment determined from the XMCD measurements (Fig. 4C) (47), including the large orbital moment. The relaxation time remains independent of pump voltage, and we conclude that the measured  $T_1$  is always that of state 1; the other states decay too quickly to be observed.

It is surprising that the pump signal is detectable for pump voltages below  $V_{02}$  because the ZFS is large, and quantum tunneling of the magnetization is forbidden in odd half-integer spin systems in the absence of a transverse magnetic field. However, the multiplet analysis shows that the weak distortion of the symmetry caused by the interaction of the Co with the Mg mixes states from higher multiplets, mostly with  $|0, \pm 1/2\rangle$  character (Fig. 4D, in red), with the lowest states  $|\pm 3, \pm 3/2\rangle$ . Although this mixing is small (on the order of 4%) and does not change the total moments substantially, it allows the coupling of states 0 and 1 by a  $\Delta S_z = \pm 1$  spin-flip transition between their  $|0, -1/2\rangle$  and  $|0, +1/2\rangle$  components, which can explain the observed quantum tunneling induced via substrate electrons. In addition, Co has a nuclear spin  $I = 7/2$ , which may facilitate otherwise prohibited electron

spin relaxation. Tunneling of the magnetization because of hyperfine coupling could explain the lack of remanence in the magnetization curve measured with XMCD. However, the hyperfine coupling is usually effective at low fields (48) and is unlikely to be the cause of the spin relaxation observed for pump-probe experiments at  $B \geq 1$  T.

The spin lifetime of Co/MgO is much lower than that reported for electrons bound to shallow donors in Si (49) as well as that reported for Ho atoms on Pt (19), both exceeding a few minutes at cryogenic temperatures. However, it is very large for a transition metal atom, for which typical  $T_1$  times are on the order of 100 ns on insulating substrates (33) and 100 fs on metals (37). This difference can be attributed to the MgO layer serving two separate purposes. First, because the binding site symmetry preserves the orbital moment, state 0 and 1 are decoupled from each other not only by the large change in spin  $S_z$ , but also by the large change in  $L_z$ . Second, even a single MgO layer is very efficient in reducing the decay of the excited state by scattering with substrate electrons. This scattering rate could be tuned by increasing the number of MgO monolayers, while still being able to electrically probe the magnetic states. Furthermore, the presence of the STM tip imposes a limit on the lifetime, and the measured 200  $\mu\text{s}$  value sets a lower bound on the intrinsic  $T_1$  of Co atoms on this surface.

### Discussion

This work elucidates the interplay between the MA, spin, and orbital degrees of freedom in systems at the border of free atoms and the solid state and highlights the atomistic limits on the miniaturization of magnetic systems. Additionally, this system realizes the single-atom analog of magnetic tunnel junctions based on perpendicular CoFeB/MgO layers. As such, it provides microscopic understanding of materials with strong perpendicular MA, which are required for further downscaling of spintronic devices (9, 10). Our measurements of ZFS and spin relaxation time demonstrate the advantages and impediments intrinsic to size reduction in such materials. Despite the very large MA, the strong coupling of  $d$ -electrons to the environment makes the spin lifetime of transition metal atoms very sensitive to perturbations caused by the ligand field and scattering from conduction electrons. Nonetheless, the large energy and time scales measured in this experiment indicate that relatively long-lived quantum states are possible for single Co atoms on MgO surfaces. Judging from the knowledge accumulated on magnetic tunnel junctions and this work, Co/MgO and possibly Fe/MgO represent a very favorable combination for the miniaturization of magnetic devices beyond the present technological limits.

On a more fundamental note, our results show that the combination of IETS and XAS is extremely powerful to describe the many-body interactions that determine the spin and the

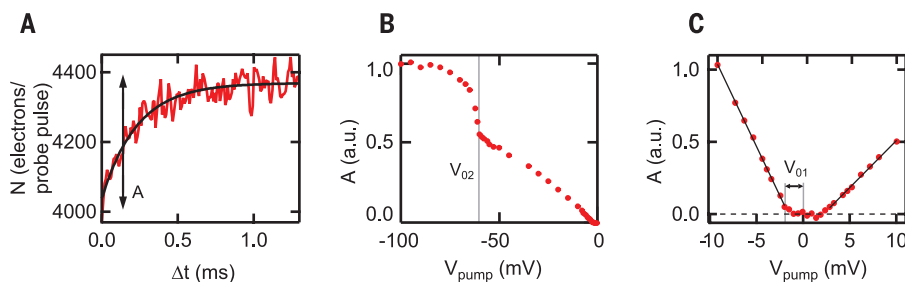


**Fig. 5. Relaxation time and excitation threshold of Co at  $T = 0.6$  K.** (A) Pump-probe measurement of the excited state relaxation time at  $B = 1$  T showing tunnel current as a function of delay time. The exponential fit (black line) yields  $T_1 = 232 \pm 17 \mu\text{s}$ . The data are taken with the tip height setpoint at  $I_{\text{set}} = 10$  pA and  $V_{\text{set}} = 100$  mV. The pulse sequence parameters are  $V_{\text{pump}} = 90$  mV,  $V_{\text{probe}} = 20$  mV. (B and C) Pump-probe signal amplitude at  $B = 3$  T as a function of pump voltage. For signal-to-noise reasons, the setpoint is  $I_{\text{set}} = 500$  pA and  $V_{\text{set}} = 100$  mV, which corresponds to the tip 0.2 nm closer to the atom than in (A). This gives  $T_1 = 7.6 \pm 0.1 \mu\text{s}$  (26). The vertical line at  $-59$  mV in (B) shows the transition seen in  $dI/dV$  spectra. (C) The pump-probe amplitude for a smaller range of pump voltages. Linear fits (black lines) extrapolate to  $-2 \pm 0.1$  mV and  $+1.8 \pm 0.2$  mV at zero amplitude. Error bars are comparable with symbol size.

orbital degrees of freedom of magnetic atoms on surfaces, going beyond the spin Hamiltonian description successfully used in previous STM studies of nanosized magnetic structures (19, 30, 32, 33). Aside from a consistent description of the electronic and magnetic ground state, the role of nonthermal spin relaxation mechanisms can be determined based on independent input obtained through the multiplet analysis of the x-ray spectra and pump-probe measurements.

## REFERENCES AND NOTES

- W. Meiklejohn, *Proc. IEEE* **74**, 1570–1581 (1986).
- P. Carcia, *J. Appl. Phys.* **63**, 5066 (1988).
- S. Khizroev, D. Litvinov, *Perpendicular Magnetic Recording* (Kluwer Academic Publishers, New York, 2004).
- S. Monso *et al.*, *Appl. Phys. Lett.* **80**, 4157 (2002).
- S. Ikeda *et al.*, *Nat. Mater.* **9**, 721–724 (2010).
- A. Manchon *et al.*, *J. Appl. Phys.* **104**, 043914 (2008).
- H. X. Yang *et al.*, *Phys. Rev. B* **84**, 054401 (2011).
- M. Cubukcu *et al.*, *Appl. Phys. Lett.* **104**, 042406 (2014).
- S. Ikeda *et al.*, *SPIN* **02**, 1240003 (2012).
- M. Gajek *et al.*, *Appl. Phys. Lett.* **100**, 132408 (2012).
- J. Z. Sun, *Phys. Rev. B* **62**, 570–578 (2000).
- Magnetic anisotropy is often defined as a classical energy barrier, or as the energy needed to orient the magnetization perpendicular to the easy-axis. Our temperature was too low to observe Arrhenius behavior because nonthermal processes dominate the relaxation in the range of temperatures accessed. Additionally, studies of quantum magnets sometimes infer a barrier using  $DS^2$  or  $DJ^2$ , but these are applicable only for pure-spin or pure-J systems. Consequently, we use the ZFS as definition of the MA.
- M. Blume, R. E. Watson, *Proc. R. Soc. Lond. A Math. Phys. Sci.* **270**, 127–143 (1962).
- J. van Vleck, *The Theory of Electric and Magnetic Susceptibilities* (Oxford Univ. Press, Oxford, 1966).
- O. Eriksson, B. Johansson, R. C. Albers, A. M. Boring, M. S. S. Brooks, *Phys. Rev. B* **42**, 2707–2710 (1990).
- D. Weller *et al.*, *Phys. Rev. Lett.* **75**, 3752–3755 (1995).
- P. Gambardella *et al.*, *Nature* **416**, 301–304 (2002).
- P. Gambardella *et al.*, *Science* **300**, 1130–1133 (2003).
- T. Miyamachi *et al.*, *Nature* **503**, 242–246 (2013).
- A. M. Bryan, W. A. Merrill, W. M. Reiff, J. C. Fettinger, P. P. Power, *Inorg. Chem.* **51**, 3366–3373 (2012).
- J. M. Zadrozny *et al.*, *Nat. Chem.* **5**, 577–581 (2013).
- J. D. Rinehart, J. R. Long, *Chem. Sci.* **2**, 2078 (2011).
- J. Klatyk *et al.*, *Phys. Rev. Lett.* **88**, 207202 (2002).
- A. Jesche *et al.*, *Nat. Commun.* **5**, 3333 (2014).
- K. Neyman, C. Inntam, V. Nasluzov, R. Kosarev, N. Röscher, *Appl. Phys., A Mater. Sci. Process.* **78**, 823–828 (2004).
- Materials and methods are available as supplementary materials on Science Online.
- S. Schintke *et al.*, *Phys. Rev. Lett.* **87**, 276801 (2001).
- S. Baumann, I. G. Rau, S. Loth, C. P. Lutz, A. J. Heinrich, *ACS Nano* **8**, 1739–1744 (2014).
- A. J. Heinrich, J. A. Gupta, C. P. Lutz, D. M. Eigler, *Science* **306**, 466–469 (2004).
- C. F. Hirjibehedin *et al.*, *Science* **317**, 1199–1203 (2007).
- A. A. Khajetoorians *et al.*, *Phys. Rev. Lett.* **106**, 037205 (2011).
- F. Donati *et al.*, *Phys. Rev. Lett.* **111**, 236801 (2013).
- S. Loth, M. Etzkorn, C. P. Lutz, D. M. Eigler, A. J. Heinrich, *Science* **329**, 1628–1630 (2010).
- F. de Groot, *Chem. Rev.* **101**, 1779–1808 (2001).
- P. Gambardella *et al.*, *Phys. Rev. Lett.* **88**, 047202 (2002).
- F. M. F. de Groot *et al.*, *J. Phys. Condens. Matter* **5**, 2277–2288 (1993).
- B. T. Thole, P. Carra, F. Sette, G. van der Laan, *Phys. Rev. Lett.* **68**, 1943–1946 (1992).
- P. Carra, B. T. Thole, M. Altarelli, X. Wang, *Phys. Rev. Lett.* **70**, 694–697 (1993).
- A. Lehnert *et al.*, *Phys. Rev. B* **81**, 104430 (2010).
- P.-O. Löwdin, *Phys. Rev.* **97**, 1474–1489 (1955).
- B. McGarvey, in *Electron Spin Resonance of Transition-Metal Complexes, Transition Metal Chemistry*, vol. 3, R. L. Carlin, Ed. (Marcel Dekker, New York, 1966).
- P. Bruno, *Phys. Rev. B* **39**, 865–868 (1989).
- J.-P. Gauyacq, N. Lorente, F. D. Novaes, *Prog. Surf. Sci.* **87**, 63–107 (2012).
- L. Thomas *et al.*, *Nature* **383**, 145–147 (1996).
- D. Gatteschi, R. Sessoli, J. Villain, *Molecular Nanomagnets* (Oxford Univ. Press, Oxford, 2006).
- R. Wiesendanger, *Rev. Mod. Phys.* **81**, 1495–1550 (2009).
- The quantum mechanical description of the energy levels derived from the multiplet calculation indicates that  $J$  is not a good quantum number. Therefore, we use the Zeeman energy ( $L_z + 2S_z$ ) $\mu_B$  instead of a description based on the Landé  $g$ -factor.
- R. Giraud, W. Wernsdorfer, A. M. Tkachuk, D. Mailly, B. Barbara, *Phys. Rev. Lett.* **87**, 057203 (2001).
- G. Feher, E. A. Gere, *Phys. Rev.* **114**, 1245–1256 (1959).

## ACKNOWLEDGMENTS

S.S. and P.G. acknowledge support from the Swiss Competence Centre for Materials Science and Technology (CCMX). J.D. acknowledges funding by an Ambizione grant of the Swiss National Science Foundation. I.G.R., S.B., C.P.L., and A.J.H. thank B. Melior for expert technical assistance. C.P.L. and A.J.H. thank the Office of Naval Research for financial support. S.G., O.R.A., and B.A.J. thank the National Energy Research Scientific Computing Center (NERSC) for computational resources. O.R.A.

## ION CHANNEL STRUCTURE

# Crystal structure of a heterotetrameric NMDA receptor ion channel

Erkan Karakas and Hiro Furukawa\*

***N*-Methyl-D-aspartate (NMDA) receptors belong to the family of ionotropic glutamate receptors, which mediate most excitatory synaptic transmission in mammalian brains. Calcium permeation triggered by activation of NMDA receptors is the pivotal event for initiation of neuronal plasticity. Here, we show the crystal structure of the intact heterotetrameric GluN1-GluN2B NMDA receptor ion channel at 4 angstroms. The NMDA receptors are arranged as a dimer of GluN1-GluN2B heterodimers with the twofold symmetry axis running through the entire molecule composed of an amino terminal domain (ATD), a ligand-binding domain (LBD), and a transmembrane domain (TMD). The ATD and LBD are much more highly packed in the NMDA receptors than non-NMDA receptors, which may explain why ATD regulates ion channel activity in NMDA receptors but not in non-NMDA receptors.**

**B**rain development and function rely on neuronal communication at a specialized junction called the synapse. In response to an action potential, neurotransmitters are released from the presynapse and activate ionotropic and metabotropic receptors at the postsynapse to generate a postsynaptic potential. Such synaptic transmission is a basis for experience-dependent changes in neuronal circuits. The majority of excitatory neurotransmission in the human brain is mediated by transmission of a simple amino acid, L-glutamate (1), which activates metabotropic and ionotropic glutamate receptors (mGluRs and iGluRs, respectively). iGluRs are ligand-gated ion channels that comprise

was supported by the National Science Foundation under grant DMR-1006605. B.A.J. thanks the Aspen Center for Physics and National Science Foundation grant 1066293 for hospitality while doing the calculations which appear in this paper. We thank A. Cavallin for helping in developing the Igor code used to analyze the XAS spectra. I.G.R., S.B., R.M.M., C.P.L., and A.J.H. performed the STM experiments and data analysis. S.G., O.R.A., and B.A.J. carried out the DFT calculations. S.R., F.D., L.G., S.B., J.D., C.P., and F.N. carried out the XMCD experiments. F.D., S.R., S.S., and P.G. analyzed the XMCD data. S.S. wrote the multiplet calculation code and performed the simulations. All authors discussed the results and participated in writing the manuscript. A.J.H., P.G., and H.B. initiated and directed this research. The authors declare that they have no competing financial interests.

## SUPPLEMENTARY MATERIALS

www.sciencemag.org/content/344/6187/988/suppl/DC1

Materials and Methods

Figs. S1 to S7

Table S1

References (50–58)

3 March 2014; accepted 21 April 2014

Published online 8 May 2014;

10.1126/science.1252841

three major families,  $\alpha$ -amino-3-hydroxy-5-methyl-4-isoxazole propionic acid (AMPA) (GluA1-4), kainate (GluK1-5), and *N*-Methyl-D-aspartate (NMDA) receptors (GluN1, GluN2A-D, and GluN3A-B). Non-NMDA receptors can form functional homotetramers that respond only to L-glutamate. In contrast, NMDA receptors are obligatory heterotetramers mainly composed of two copies each of GluN1 and GluN2, which activate upon concurrent binding of glycine or D-serine to GluN1 and L-glutamate to GluN2 and relief of a magnesium block of the ion channel pore by membrane depolarization (2). Opening of NMDA receptor channels results in an influx of calcium ions that triggers signal transduction cascades that control the strength of neural connectivity or neuroplasticity. Hyper- or hypo-activation of NMDA receptors is implicated in neurological disorders and diseases including Alzheimer's

Cold Spring Harbor Laboratory, W. M. Keck Structural Biology Laboratory, One Bungtown Road, Cold Spring Harbor, NY 11724, USA.

\*Corresponding author. E-mail: furukawa@cshl.edu



## Supplementary Material for

### **Reaching the Magnetic Anisotropy Limit of a $3d$ Metal Atom**

Ileana G. Rau, Susanne Baumann, Stefano Rusponi, Fabio Donati, Sebastian Stepanow, Luca Gragnaniello, Jan Dreiser, Cinthia Piamonteze, Frithjof Nolting, Shruba Gangopadhyay, Oliver R. Albertini, Roger M. Macfarlane, Christopher P. Lutz, Barbara Jones, Pietro Gambardella,\* Andreas J. Heinrich,\* Harald Brune\*

\*Corresponding author. E-mail: andreash@us.ibm.com (A.J.H.); pietro.gambardella@mat.ethz.ch (P.G.); harald.brune@epfl.ch (H.B.)

Published 8 May 2014 on *Science Express*  
DOI: 10.1126/science.1252841

**This PDF file includes:**

Materials and Methods

Figs. S1 to S7

Table S1

Full Reference List

# Contents

<b>Sample Preparation</b> .....	3
<b>Extended explanation of DFT Method</b> .....	3
Analysis of Charge and Spin densities (see Figures 1B and 1D in the main text).....	4
Extended Analysis of Density of States (see Figure 2 in the main text).....	4
Extended Orbital Analysis .....	5
<b>STM and IETS methods</b> .....	6
Fits to IETS data.....	6
Spin polarized pump-probe measurements.....	8
<b>Extended description of the x-ray absorption measurements</b> .....	9
Charge transfer multiplet calculations .....	11
<b>Agreement between multiplet picture and IETS measurements</b> .....	15
Mapping the ground state multiplet onto an effective Hamiltonian.....	15
Upper limit of the zero field splitting.....	17
<b>Full List of References and Notes</b> .....	18

## Sample Preparation

In STM and XAS experiments, the sample preparation began with repeated sputter / heating cycles of the Ag(100) single crystal samples. Once a high-purity metal surface was achieved, Mg was evaporated from a crucible in an O<sub>2</sub> environment ( $p_{\text{O}_2} = 1 \cdot 10^{-6}$  mbar). We employed growth rates of 1 ML per minute at a sample temperature of typically 350°C. The MgO on Ag samples were then transferred in vacuum into a low-temperature system for the deposition of Co at about 5-10 K. Measurements were performed at 0.6 to 1.2 K in the STM and 3.5 K in the XAS setup and in magnetic fields up to 6.8 T.

## Extended explanation of DFT Method

Spin-polarized DFT was used, as implemented in Quantum ESPRESSO(50) and WIEN2k(51).

The Quantum ESPRESSO calculations were performed within a pseudopotential formalism using a plane wave basis with a cutoff of 60 Ry. A higher cutoff of 480 Ry was used for the augmentation charges introduced by the norm conserving pseudopotential. We use the generalized gradient approximation (GGA) for the exchange correlation interaction with Perdew-Burke-Ernzerhof functional. To improve convergence, a Gaussian smearing of width 0.01 Ry was adopted for geometry optimization. For single point DFT+U calculations we used Gaussian smearing of width 0.0001Ry. To minimize the Brillouin zone integrations for the (3 x 3) surface cell calculations were carried out using a (8x8x1) mesh of k points. We use a slab of 6 atomic layers of Ag, in which the lower 3 are kept fixed at bulk Ag values. On top of this we put a layer of MgO where Ag stays underneath O as determined theoretically(52) (followed by experimental confirmation) and on an O site (the most stable) we place a Co atom. Above the slab are 8 effective atomic (Ag) layers thick of vacuum. This structure is repeated periodically in the z-direction. The x and y directions are thus in the plane. Part of our unit cell appears in Figure 1B, of the main text. The crystal structure is optimized until the maximum force among the atoms reduces to  $< \sim 10^{-3}$  Ry/a<sub>0</sub>, and with an energy accuracy of 10<sup>-4</sup>.

The WIEN2k calculations were carried out with an inversion symmetric 7 layer structure, which includes 5 layers of Ag, and a top and bottom layer of MgO. The slab was set up with 8 layers of vacuum between the top and bottom adatoms. The structure was optimized so that calculated forces on all atoms were less than 2 mRy/a<sub>0</sub>. The energy cut-off as implemented in WIEN2k is represented by the parameter  $R_{\text{mt}}K_{\text{max}}$ , was 7 in these calculations. A temperature broadening was applied to the eigenvalues according to the Fermi function with  $\Delta E=0.001$  Ry. We use the generalized gradient approximation (GGA) for the exchange correlation interaction with Perdew-Burke-Ernzerhof functional. The calculations were carried out using a 13x13x1 k-point mesh.

Because a naïve application of DFT on *d*-electron materials generally does not get either the *d*-electron energy correct or many aspects of the magnetization, we used an on-site Coulomb interaction ( $U$ ) for the *d*-states of the Co. Calculating the  $U$  using WIEN2k using a constraint-GGA method gives a  $U$  which is much too small. This is reminiscent of previous calculations of Co on another surface,  $\text{Cu}_2\text{N}/\text{Cu}$ . There, a Kondo effect occurs because of the strong hybridization with the Cu substrate, and an argument is made to not use a Coulomb interaction, since a dynamic effect is taking place. In the case of the system under discussion in this paper, MgO is a much more efficient insulator, and no Kondo effect takes place. Instead, the magnetism of Co is fully evident; however, as will be discussed below, there is still evidence for considerable hybridization with the surface. In cases with large hybridization with neighboring atoms, the constraint-GGA method for calculating  $U$  is less accurate. Instead, we utilized Quantum ESPRESSO and calculated  $U$  by using a linear response approach that is internally consistent with the chosen definition for the occupation matrix of the relevant localized orbitals. We obtained  $U$  as 6.9 eV using this method which is consistent with  $U$  used for cobalt oxide.

We created the electron density plots using WIEN2k and XCrysDen. The DOS was also calculated with WIEN2k, using the all-electron (L)APW(+local orbital) methods with the PBE exchange correlation potential (GGA). The same  $U$  and optimized structure was used for both calculation methods. The atomic charges were calculated using the Bader Atom in Molecule (AIM) scheme, as implemented in the WIEN2k code. The Bader definition of the atomic surface is that for which the electronic flux is zero ( $\vec{\nabla}\rho \cdot \hat{n} = 0$ ). Using this definition, we find that the Co atom on O is essentially neutral.

### **Analysis of Charge and Spin densities (see Figures 1B and 1D in the main text)**

Our calculations of charge density reveal the strong interaction between the Co and the O beneath it (nearest neighbor O). To a lesser degree, there is some interaction between Co and Mg as well as between Co and its next nearest neighbor O.

Charge is transferred from the Mg to neighboring O atoms, in a manner similar to bulk MgO where O, lacking just two electrons to complete its octet, strongly attracts electrons from Mg. Therefore, the O underneath the Co attracts most of its charge from the Mg atoms and a much smaller amount from the Co. Mg, with two valence *s*-electrons, hybridizes with both the O and the Ag in the substrate.

### **Extended Analysis of Density of States (see Figure 2 in the main text)**

Because the cobalt *d*-levels are close to the O *p*-level energies in this material, there is strong interaction and hybridization with the O.

The lowest-energy *d*-orbital peak at -7 eV comes from  $d_{z^2}$  of Co and  $p_z$  of O. This sigma bonding of *p* and *d* orbitals explains the sigma donation from  $d_{z^2}$  Co to  $p_z$  O. Due to this hybridization, those orbitals on the Co are no longer pure  $d_{z^2}$  character. The spin density at this energy (Fig. 1D in the main text) illustrates the nearly cylindrical symmetry in the *z*-direction and shows the formation of a molecular orbital between Co and O.

The next degenerate orbitals at -6.5 eV come from  $d_{xz}$  and  $d_{yz}$  hybridized with  $p_x$  and  $p_y$  orbitals of oxygen, forming a  $\pi$ -bonding orbital. Even in the unoccupied orbitals one can see a correspondence between the Co and the O. This is in contrast with the case of the bare MgO surface, or for oxygen atoms far from the Co, which exhibit roughly equal weight of  $p_x$ ,  $p_y$ , and  $p_z$  (not shown).

### Extended Orbital Analysis

**Table S1.** Löwdin population analysis of number of electrons of Co/MgO/Ag system, for Co only the spin is noted. All the atoms referred according to Figure S1. Löwdin spheres only include electrons in the occupied orbitals surrounding an atom, and leave out interstitial electrons. A Löwdin charge analysis allows projections onto atomic orbitals. A Bader calculation, based on the electron density, is in contrast space-filling, and includes all interstitial electrons. The Interstitial row in the table below represents the difference between a Bader and Löwdin analysis. The Charge row represents the Bader result. We note the negative charge for the Mg, which is due to the very large  $3s$   $3p$   $3d$  basis used for the Löwdin analysis for this atom.

Number of valence electrons						Spin
	Co	O <sub>1</sub>	O <sub>2</sub>	Mg	Ag <sub>1</sub>	Co
<i>s</i>	0.97	1.56	1.63	0.28	0.69	0.04
<i>p</i>	0.53	4.82	5.02	0.82		0.08
<i>d</i>	7.27			0.85	9.85	1.39
<b>Tot</b>	<b>8.77</b>	<b>6.38</b>	<b>6.65</b>	<b>1.95</b>	<b>10.54</b>	<b>1.51</b>
<b>Interstitial</b>	<b>0.14</b>	<b>1.21</b>	<b>0.99</b>	<b>-1.65</b>		
<b>Charge</b>	<b>+0.09</b>	<b>-1.59</b>	<b>-1.64</b>	<b>+1.70</b>	<b>+0.46</b>	

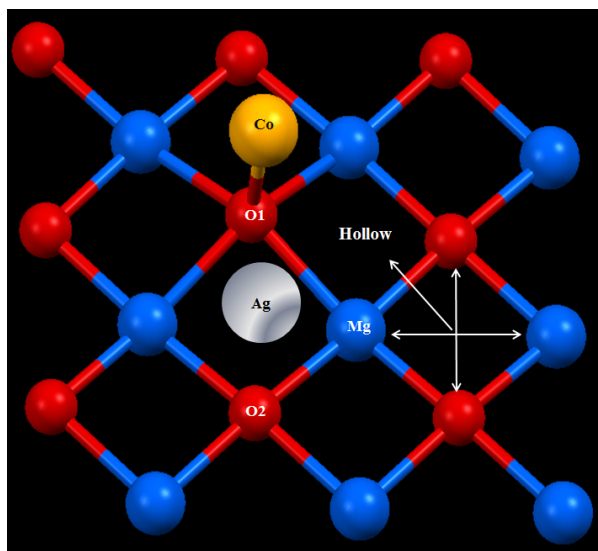


**Figure S1** | Oxygen top geometry of Co/MgO system, only one Ag is shown, this figure showing three possible sites, O top, Mg top and hollow.

At -2.75 eV for spin up and at -1.25 eV for spin down,  $d_{xy}$  and  $d_{x^2-y^2}$  are almost pure  $d$  levels. The coupling with nearest-neighbor O is small, and their small asymmetry arises solely from the interactions with the nearest-neighbor Mg and next-nearest-neighbor O.

In table S1 we see the occupancy of the various orbitals of the Co and its surrounding atoms. Atomic Co has 2  $s$  electrons and 7  $d$  electrons. On the MgO surface, Co has more than 7  $d$  electrons, closer to 7.3 or 7.4 as noted in the main text. The net is still charge neutral, in the Bader volume, although slightly positively charged in the Löwdin sphere as seen in the table. DFT finds the extra  $d$ -weight (beyond the  $d^7$  configuration) on the Co to come from depopulating the  $s$ -level, down to one  $s$  electron (from the  $3d^74s^2$  configuration of a free Co atom). The missing  $s$  electron goes half to a  $p$ -type shell shared with the O, and roughly half to the  $d$ . This movement of electrons out of  $s$  comes about because of hybridization with the underlying O, which mixes the  $4s$  and  $3d$  energies, which are very close for the bare Co. Some of the weight of the extra electrons in the  $d_{z^2}$  shell of the Co and the  $p_z$  shell of O are found in the interstitial region between the O and the Co, accounting for the difference between the Löwdin and Bader analyses. DFT+U finds the spin of the Co to be close to 3/2.

## STM and IETS methods

STM measurements were performed at the IBM Almaden laboratory in a ultra-high-vacuum low-temperature system(29). We performed IETS measurements by applying a DC voltage between the STM tip (positioned over the Co atom) and the sample and measuring the conductance using a lock-in technique with a 150  $\mu$ V, 806 Hz AC excitation. For inelastic excitations, it is generally observed that when the applied DC voltage is below a threshold of excitation the conductance is constant, but a sudden increase in conductance is observed when the applied voltage is increased above this excitation energy(29,53).

Spin-polarized experiments were performed in the same microscope. We generated spin-polarized STM tips by transferring magnetic atoms to the tip apex and applying a magnetic field to polarize those atoms on the tip(33). This technique allows us to study the same atom on the surface with tips with different degrees of spin-polarization.

In pump-probe measurements a pump-pulse with a voltage above an excitation threshold is used to generate a non-equilibrium population of spin states(33). A probe pulse of lower voltage is then applied at variable delay and the tunnel current due to the probe pulse is measured as a function of the delay between pump and probe. If the delay is long enough, the system will have recovered into the ground state ( $S_z = -3/2$ ) before the next pump pulse arrives.

### Fits to IETS data

For the low field data, where only one step is visible, we extract the position  $V_{\text{IETS}}$  and the width of the IETS transition by fitting the expected IETS functional form(54). Small differences between the absolute conductance measured are due to small experimental variations in the height of the tip above the atom. We scale the conductance by the step

height to make the different magnetic field data directly comparable. Fig. S2a shows a 0T (red trace) and 2T (green trace) zoom-in of the IETS step and the corresponding fit with the step height, position and width, and vertical offset as fitting parameters. The fitted  $V_{\text{IETS}} = 57.7$  mV is the same for the two magnetic fields to within a systematic error of  $\pm 0.03$  mV due to instrument drift.

The fitted width of the 0T step is 1.5 meV. This width corresponds to  $5.5 k_B T$  in the case of a thermally broadened IETS transition, giving  $T=3.1$  K. The 2T fit is wider and results in  $T=3.6$ K. In both cases, the extracted equivalent temperature is larger than the 0.6-0.7 K measurement temperature. We have excluded the applied AC voltage as a possible broadening source: varying the rms value does not affect the transition width. We have also excluded the possibility of other broadening sources such as heating or RF noise: on the same sample and with the same tip, the IETS transition width of neighboring Fe atoms corresponds to  $T < 2$ K. This indicates that this width is “native” to measuring the Co atom.

The scaled 4T and 6T spectra with a faint double step at 4T and a clear double step at 6T are shown in Fig. S2b. To determine the position and width of the two separate steps at large magnetic field we fit the sum of two IETS transitions with the same width. Fig. S2c, shows what such a fit to the 6T spectrum looks like for 3 different fixed widths. The

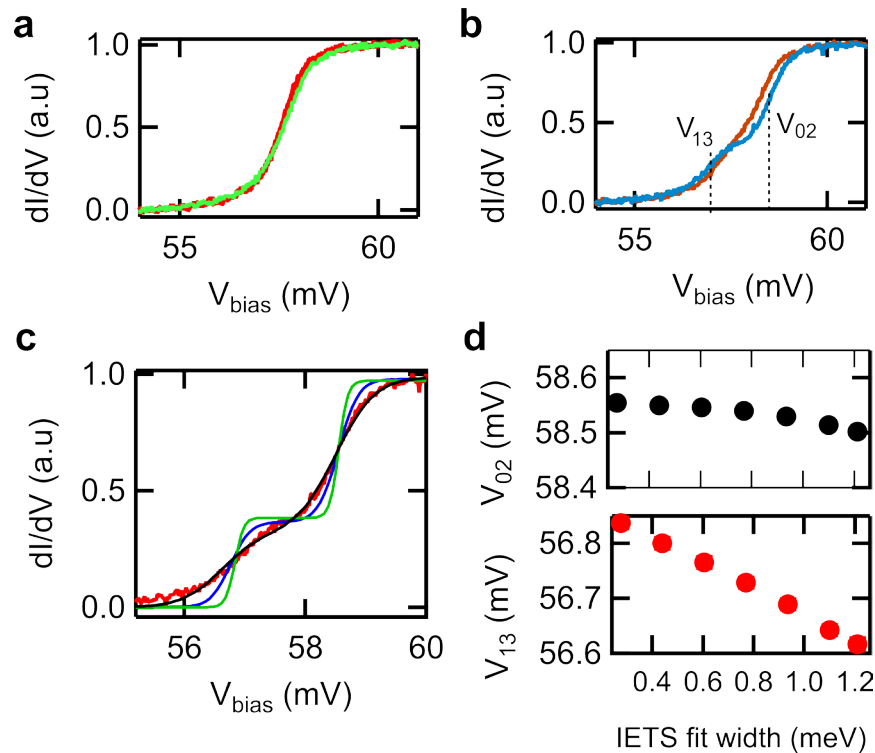


**Figure S2| Step positions of spin excitations as function of B.** **a**, IETS step at 0T (red) and 2T (green). **b**, IETS step at 4T (brown) and 6T (blue). The transition energies corresponding to the two steps are indicated with dashed lines. **c**, Zoom-in of the IETS spectrum at 6 T (red) and the corresponding three fits to the sum of two IETS functions with fixed widths: 1.2 meV (black), 0.6 meV (blue), 0.3 meV (green). **d**, The position of the first step (bottom) and of the second step (top) extracted from the fit to the 6T data, as a function of the fixed IETS fit width.

heights of the steps were allowed to vary independently. Interestingly, the width of the separate steps at 6T corresponds to  $T=2.3\text{K}$  which is smaller than the 0T step width.

We ensure that the extracted step positions are robust against changes in the fitting parameters by using two fitting procedures. First we compare the fitting parameters using the sum of two IETS functions for the uncorrected data as well as for the data with a linear background subtracted and we do not see a change outside the error bars of the fit. Second, we fit the sum of two IETS functions to the uncorrected data for several different fixed widths ranging from 0.6K to 3K. The resulting fit IETS step positions are shown in Fig. S2d (the error bars on the individual values are of the size of the markers). The first step position varies by 0.22 meV while the second step varies by 0.06 meV over this range of fixed fit widths. For the larger width, the position of the step is not correctly determined by the fit. In order to force the fit to identify the middle of each step reliably, use a fixed width that underestimates the true width of the steps. For the extracted step positions used in the main text the fit width employed is 0.11meV ( $=1.3\text{K}$ ) and the difference between the step positions is  $1.8\pm 0.2$  meV. The error bar is based on the variation in the step position value with the fixed width in the range described above.

### Spin polarized pump-probe measurements

Our pump-probe measurement scheme allows the measurement of the relaxation time ( $T_1$ ) of our spin system. A pump voltage pulse places the atom into excited magnetic states, and probe voltage pulses sense the magnetic state as a function of the delay  $\Delta t$  after the preceding pump pulse. A Co or Fe atom is transferred to the microscope tip and polarized by the applied magnetic field to yield a spin-polarized tip. Because the tunnel current depends sensitively on the relative alignment of the tip and sample spins, this technique distinguishes between the surface atom being in the ground or excited state. An exponential fit to the pump-probe signal is used to measure relaxation time.

The data in Fig. 5A of the main text is taken at 1 T with the tip height setpoint at  $I_{\text{set}} = 10$  pA and  $V_{\text{set}} = 100$  mV. The pulse sequence parameters used are:  $V_{\text{pump}} = -90$  mV,  $V_{\text{probe}} = -20$  mV, pump (probe) width 350  $\mu\text{s}$ .

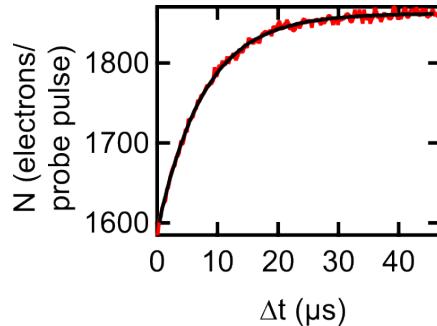


**Figure S3 | Relaxation time used for the threshold measurement.** a, Tunnel current as a function of pump probe delay at the same conditions as Fig. 5B,C of the main text, setpoint  $I=500\text{pA}$  and  $V=100\text{mV}$ ,  $B = 3$  T, on the same atom and with the same tip as in main text Fig. 5B,C. Exponential fit (black trace) gives  $T_1 = 7.6 \pm 0.1$   $\mu\text{s}$ .

To measure  $V_{01}$  in Fig. 5B,C of the main text, we applied a larger magnetic field, 3T, in order to more clearly resolve  $V_{01}$ . For signal to noise reasons, the setpoint is  $I_{\text{set}} = 500$  pA and  $V_{\text{set}} = 100$  mV, which corresponds to the tip  $\sim 0.2$  nm closer to the atom than for a setpoint of  $I_{\text{set}} = 10$  pA and  $V_{\text{set}} = 100$  mV used in Fig. 5A. The pulse sequence parameters used are:  $V_{\text{pump}} = -90$  mV,  $V_{\text{probe}} = -10$  mV, pump (probe) width 15  $\mu\text{s}$ . The measured relaxation time does not depend on variations in the pump or probe voltage (nor on the pump or probe width), but the decreased tip-atom distance and different applied magnetic field results in a shorter lifetime. The lifetime corresponding to the settings used to measure the data in Fig. 5B,C is 7.5  $\mu\text{s}$  and is shown in Fig. S3.

For high signal-to-noise, the pump-probe signal is modulated at audio frequency (20 – 900 Hz) and detected using standard lock-in techniques. For Fig. 5A in the main text and Fig. S3, a “probe chop” technique is used, in which the probe pulses are present at delay time  $\Delta t$  during the first half of each audio cycle, and absent during the second half. For Fig. 5B,C a “probe shift” technique applies probe pulses at delay  $\Delta t$  during the first half of each audio cycle, and at fixed long delay  $\Delta t_0 \gg T_1$  during the second half. In all cases, the series of pump pulses continues uninterrupted through both halves of the audio cycle and consequently produce no signal at the audio modulation frequency.

We note that in Fig. 5C of the main text, the difference in the slope of the signal at positive versus negative pump voltage is due to the spin-polarization of the tip.

## Extended description of the x-ray absorption measurements

The x-ray experiments were performed at the X-Treme beamline of the Swiss Light Source (SLS)(55) using circularly polarized light at a temperature of  $3.5 \pm 0.5$  K and in magnetic fields up to 6.8 T. The samples were prepared in-situ by deposition of Mg with a partial pressure of  $1 \times 10^{-6}$  mbar of  $\text{O}_2$  at room temperature on a clean Ag(100) single crystal surface. The MgO coverage, calibrated by in-situ STM, was chosen to be between 2 and 4 monolayers in order to ensure the complete coverage of Ag by MgO. Co was deposited directly in the XMCD cryostat from high-purity rods (99.995%) using a mini e-beam evaporator. The sample temperature was kept at 3.5 K during deposition to avoid surface diffusion and cluster formation. During deposition the pressure in the XMCD cryostat remained below  $5 \times 10^{-11}$  mbar. The Co coverage was calibrated using the absorption intensity at the Co  $L_3$  edge measured on reference samples for which the Co coverage was determined by STM. Different samples with Co coverage ranging from 0.03 to 0.10 monolayers were measured.

The x-ray absorption spectra (XAS) were recorded in the total electron yield (TEY) mode and normalized by the intensity of the x-ray beam measured on a metallic grid placed upstream from the sample. The XAS were measured with the magnetic field applied collinearly with the photon beam at normal ( $\theta = 0^\circ$ ) and grazing incidence ( $\theta = 60^\circ$ ). The XMCD signal is the difference of XAS recorded for parallel ( $I^+$ ) and antiparallel ( $I^-$ ) alignment of the photon helicity with the applied magnetic field. Due to the small coverage, the Co absorption intensity is small and superimposed to a large background signal originating mostly from the excitation of the Ag  $M$ -edges (inset in Fig. S4a). This

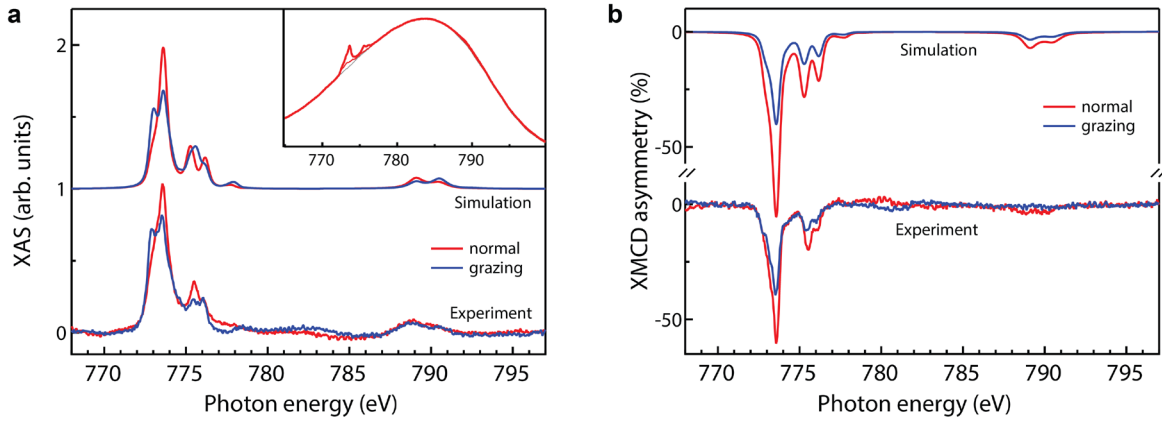


**Figure S4** | **a**, Measured and simulated x-ray absorption spectra of  $\text{Co}_1/\text{MgO}/\text{Ag}(100)$  at normal ( $\theta=0^\circ$ ) and grazing ( $\theta=60^\circ$ ) incidence recorded over the  $L_{2,3}$  edges at  $T = 3.5$  K and  $B = 6.8$  T. The spectra shown in **a** are the sum of plus and minus polarization ( $I^+ + I^-$ ). The inset shows the  $I^+$  (red solid line) and  $I^-$  (red dashed line) absorption spectra at normal incidence before background subtraction (gray line). **b**, XMCD spectra obtained in the same conditions. The XMCD intensity is given as percentage of the total absorption signal shown in **a**.

background was measured prior to the deposition of Co and subsequently subtracted from the XAS in order to facilitate the analysis of the multiplet features and compare it with the spectra calculated using the charge transfer multiplet model.

XAS measurements of metal atoms on thin insulating layers present technical challenges related to the low concentration of the atoms to be probed as well as to the x-ray induced desorption of the adatoms. We found that the XAS intensity quickly changed as a function of time due to exposure to the x-ray beam. Whereas the spectral shape remained mostly unchanged, the absolute absorption intensity at the Co edge was strongly decreasing, by about 20% in 120s, which is the time required to measure a single absorption scan. When moving the x-ray beam over the sample to a new region, which had not been exposed before, the XAS and XMCD intensities recovered to the original value. Note that the change in the absorption intensity was not reversible, which was verified by temporarily switching off the x-ray beam and recording a spectrum again after a few minutes. Because the spectral lineshape remains the same, we exclude that this effect is due to a change of coordination of the Co atoms induced by diffusion and aggregation, which would imply significant broadening and changes of the XAS multiplet features(36). Therefore, the intensity reduction with exposure time must be attributed to a decrease of the Co coverage due to photon induced adatom desorption, as already observed for Co monomers deposited on  $\text{Al}_2\text{O}_3$ (39). For this reason, every x-ray absorption spectrum was measured on a different region of the sample using a defocused x-ray beam spot size of 1.5 mm x 0.8 mm. The XAS shown in the manuscript are averages of two  $I^+$  and two  $I^-$  spectra recorded over four different regions. Although the Co coverage is homogeneous on the dimensions of the substrate (round crystal with 7 mm diameter), this procedure severely limits the acquisition time for each sample and introduces errors in the determination of the absolute XAS intensity required to extract the magnetic moments using the XMCD sum rules(37,38).

The orbital magnetic moment estimated by applying the sum rules to the spectra measured at normal incidence at 6.8 T and 3.5 K is  $0.9 \mu_B/\text{hole}$ . This gives  $\langle L_z \rangle = 2.43 \mu_B$  using the number of  $3d$  holes calculated by DFT (2.78) and  $2.30 \mu_B$  using the number of holes in the multiplet simulations (2.56). As mentioned above, these values are affected by the x-ray induced desorption of Co from the MgO surface and consequent limitations on the signal-to-noise ratio. The subtraction of the MgO background introduces additional uncertainty in the determination of the total absorption intensity. Given the different error sources, we estimate that the uncertainty of  $\langle L_z \rangle$  determined by the orbital moment sum rule is of the order of 20%. The multiplet simulations of the XAS lineshape as well as the Zeeman splitting measured by IETS and the large ZFS, however, provide a more precise estimate of  $\langle L_z \rangle$ , close to  $3 \mu_B$ . In the manuscript, we report the effective spin moment ratio,  $\langle L_z \rangle / (2 \langle S_z \rangle + 7 \langle T_z \rangle)$ , where  $\langle T_z \rangle$  is the spin dipole moment (38), which depends only on the XMCD lineshape and is less affected by changes of the absorption intensity as well as by the MgO background subtraction.

Magnetization curves versus applied field (Fig. 4C, main text) were measured at normal incidence by saturating the magnetic moment at 6.8 T and recording a pair of spectra  $I^+$  and  $I^-$ , with each spectrum taken on a different sample position. Because of the need to measure spectra at different points and the larger footprint of the x-ray beam at  $\theta = 60^\circ$ , it was not possible to measure the magnetization versus field at grazing incidence.

### Charge transfer multiplet calculations

The XAS simulations are based on an atomic multiplet model that takes into account the electron-electron interaction among  $d$ - and  $p$ -electrons using rescaled Slater-Condon integrals, and the atomic spin-orbit interaction (56). The atomic environment is simulated by the crystal field potential generated by the surrounding bonding atoms. The finite overlap of the metal wavefunctions with the ligand atoms (covalency) as well as charge fluctuations in the initial and final states are described by extending the atomic multiplet model to configurational interaction. In such a scheme, in addition to the correlated state of the central atom one considers an additional (delocalized) state or band outside the atom that is generally localized on the ligands(57). The coupling of this state to the central atom is enabled via a hopping term that effectively annihilates an electron or hole at the ligand orbital and recreates it at the atom site. Different pathways can be distinguished for the hopping term, i.e., electrons can be allowed to hop only onto specific orbitals within the  $d$ -shell. Thus the particular symmetry and overlap with the ligand orbitals can be explicitly taken into account. For the calculations the full spectrum of the LS terms is considered. For instance, for a  $3d^7$  configuration this yields 120 different determinantal states, while the final state configuration  $2p^5 3d^8$  has  $6 \times 45 = 270$  different states. Not all of these final states have finite intensity, depending on the selection rules (see below). The full Hamiltonian for the initial and final state is diagonalized considering all contributions (electron-electron interaction, ligand field, spin-orbit coupling and magnetic field) simultaneously using Lapack routines written in Fortran. This yields wavefunctions and energies from which we calculate also the expectation values of the spin and orbital moments. Our code is free of symmetry restrictions, i.e., external fields can be applied in any possible direction.

For calculating the intensity  $I$  of the x-ray absorption spectra we use the dipole approximation within Fermi's Golden rule,

$$I \propto \sum_f |\langle f | C_1^q | i \rangle|^2 \delta(E_f - E_i - \hbar\omega). \quad (1)$$

Here,  $C_1^q$  is the dipole operator corresponding to photons with polarization  $q = \pm 1$  (for circularly polarized light),  $|i\rangle$  and  $|f\rangle$  the initial and final states of energy  $E_i$  and  $E_f$ , respectively, and  $\hbar\omega$  the x-ray photon energy. Such an expression involves two separate calculations, one for the initial state configuration, e.g.,  $2p^6 3d^7$ , and the corresponding final state configuration including a  $2p$  core hole and an additional electron in the  $d$ -shell,  $2p^5 3d^8$ . The Coulomb interaction between the core-hole and valence electrons is included and accounts for the multiplet features observed in the XAS spectrum. The sum in Eq. (1) is performed over all states of the final state configuration that are dipole-allowed starting from the ground state. At finite temperature, the population of excited states of the initial state configuration is also taken into account by considering transitions from Boltzmann weighted initial states. In order to compare the calculated spectra with the experimental ones, the transition amplitudes at the  $L_2$  and  $L_3$  edges are broadened by a Lorentzian function with FWHM of 0.45 and 0.15 eV, respectively. The  $L_2$  edge has a stronger broadening since the atomic transitions interact with the continuum transitions of the  $L_3$  edge. Finally, the spectrum is further broadened by a Gaussian function with 0.35 eV FWHM to account for the experimental energy resolution.

The ligand field and hopping parameters as well as the charge transfer energy are determined by systematically varying their values in increasingly narrow energy intervals, starting from an educated guess of their range. The Slater-Condon integrals are rescaled by 75% because of the overestimation of the Hartree-Fock value and a further reduction due to chemical bonding. The value of the one-electron spin-orbit coupling constant of Co is taken to be  $\xi=66$  meV(13). The charge transfer energy between the initial state configurations  $\Delta=E(d^7)-E(d^8)$  was set to -1.25 eV. The final state value is 1 eV lower due to the stronger core-hole attraction compared to the  $dd$  repulsion. The agreement between calculated and experimental x-ray absorption spectra is considered to be satisfactory when the simulations correctly reproduce the number and position of the multiplet features as well as the relative intensity of the spectra measured at normal and grazing incidence and the XMCD intensity. From the simulations, we obtain the many-electron wavefunctions and corresponding energies for the initial and final states. Only the initial state properties are relevant to determine the magnetic behavior of the system and compare XAS and STM data.

For the Co/MgO(100) system, the  $\sigma$ -type bond to the substrate O atom generates an axial (cylindrical) crystal field, which we model using the parameters  $D_s = -0.11$  and  $D_t = -0.008$  eV. Considering further the  $C_{4v}$  symmetry of the adsorption site, we allowed for the  $d_{x^2-y^2}$  orbital to interact weakly with the empty Mg states (backbonding) by including a small cubic field of amplitude  $10D_q=-0.1$  eV. According to the DFT results, the occupation of the  $d$ -shell of the Co ground state configuration is about 7.3 electrons, see table S1. To account for this, we took into account charge transfer ( $\sigma$ -donation) between Co  $d$ -state and O  $2p$ -states via the  $d_{z^2}$  orbital, by considering the mixing between  $d^7$  and

$d^8l$  configurations, where  $l$  describes a ligand hole on the O site. As shown in Fig. S4, we find excellent agreement between the simulated and experimental XAS and XMCD spectra. The  $d$ -shell occupancy is 7.44 electrons, which signifies a substantial mixing of the  $d^7$  and  $d^8$  configurations. The ground state symmetry is E with an orbital occupation of  $(b_1)^{1.62}(b_2)^{1.38}(e)^3(a_1)^{1.44}$ . The ground state doublet has an exceptional high orbital moment of  $L_z=2.9 \mu_B$  and a spin moment of  $S_z=1.27 \mu_B$ , which are very close to the values expected for the  $^4F$  ground state of a free Co atom.

To understand the preservation of the atomic-like orbital moment it is useful to follow the evolution of the energy levels by considering the effects of charge transfer, crystal field, spin-orbit coupling, and Zeeman splitting in successive steps, see Fig. S5. Charge transfer between O and Co has the strongest influence on the energy levels. Figure S5a shows the energy levels of the atomic multiplet calculations for pure  $d^7$  and  $d^8$  configurations when only electron-electron interactions are present. The ground state terms ( $^4F$  and  $^3F$ ) of the  $d^7$  and  $d^8$  configurations are close in energy and have the same orbital moment,  $L=3$ . Mixing of the two configurations splits the atomic multiplets in energy. Such a splitting is shown in Fig. S5b as the hopping between the two configurations is varied from zero to the final value of  $t=0.75$  eV. The three lower levels, corresponding to those enclosed by a dashed square in Fig. S5a, are the starting points for the diagram reported in Fig. S5c. The ground state of the mixed  $d^7+d^8l$  configuration is an octuplet with  $L_z=\pm 3 \otimes S_z=\pm 1.25, \pm 0.42$ . The next higher lying states are a quadruplet ( $B_2$  character) with  $L_z=0$  and an octuplet (E symmetry) with  $L_z=\pm 1$ . As shown in c, this picture does not change after the application of the axial crystal field (note that hopping via the  $a_1$  ( $d_{z^2}$ ) orbital also acts as an effective axial field as it pulls the  $|L_z|=3$  states down). The reduced spin moments are a result of the mixing of the spin quadruplet and triplet from the ground state  $^4F$  and  $^3F$  terms of the  $d^7$  and  $d^8$  configuration, respectively. The orbital moment however is not quenched and has the same magnitude as in the free atom case. This can be understood by two facts. First, the axial field is not able to lift the degeneracy between the  $|m_L|=1$  and  $|m_L|=2$  states of the  $d$ -shell and, second, both  $d^7$  and  $d^8$  configurations have the same orbital multiplicity. This shows that Co is the best suited  $3d$  transition-metal ion to obtain large orbital moments since configuration mixing, which takes place on most substrates, does not reduce its magnitude. The effect of the cubic term is to lift the degeneracy between the  $b_2$  ( $d_{xy}$ ) and  $b_1$  ( $d_{x^2-y^2}$ ) orbitals due to a small overlap of the  $b_1$  state with empty Mg orbitals. As expected, the orbital moment is partially quenched but remains high ( $L_z=2.86$ ) for the ground state octuplet. Finally, spin-orbit coupling is introduced, leading to a relatively strong splitting of the energy levels and a crossing with the excited state quadruplet. The energy levels and corresponding moments are shown in Figure S5d. The ground state octuplet, essentially made up from  $L=\pm 3 \otimes S=\pm 3/2, \pm 1/2$  states, is maximally split by the spin-orbit interaction thanks to the almost fully unquenched orbital moment of these states. Mixing with the low lying  $B_2$  excited state modifies the orbital and spin moments and affects the character of the ground state octuplet, but only to a small extent. The ground state found here is robust for a broad range of crystal field values and the separation of the first two spin doublets is always of the order of  $\sim 60$  meV.

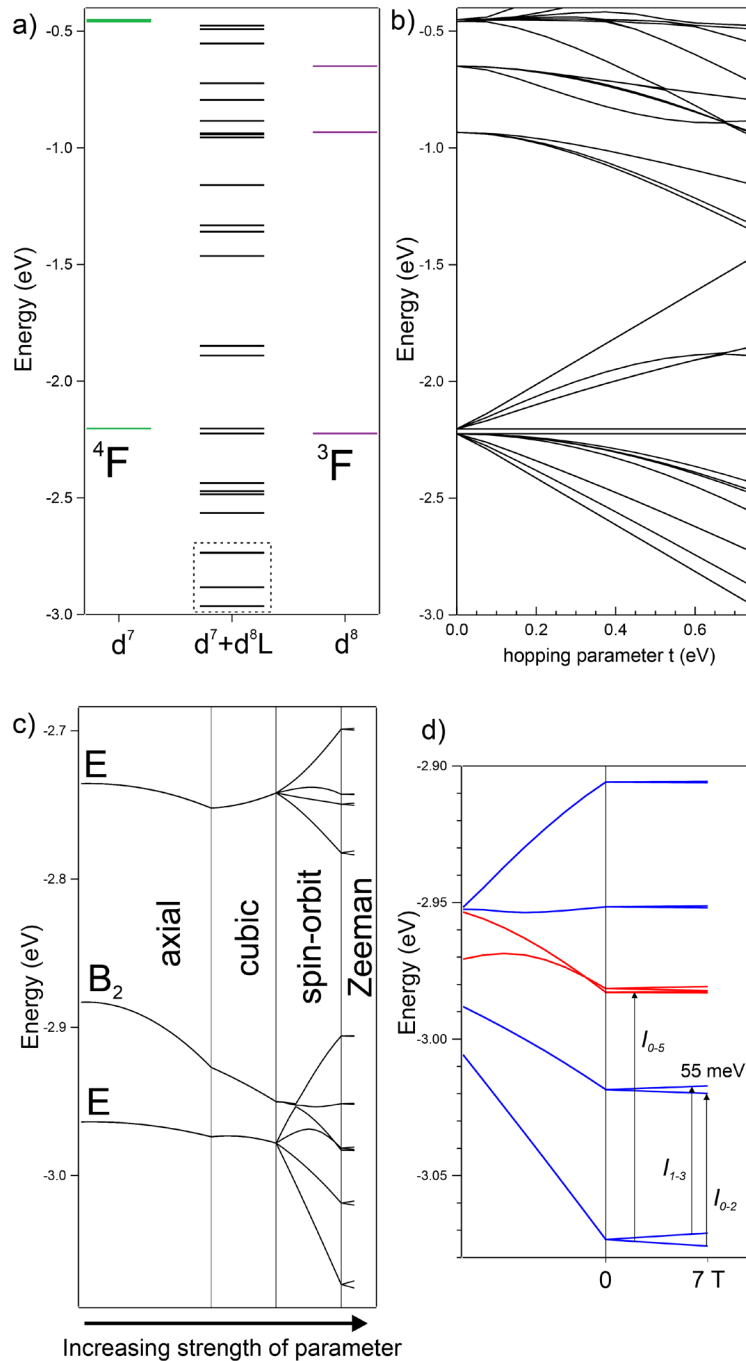


**Figure S5| Energy levels obtained by the multiplet calculations.** **a**, Energy levels of the pure atomic multiplets for the parent  $d^7$  and  $d^8$  configurations and when mixing via the hopping term. **b**, Evolution of the energy levels of the mixed  $d^7+d^8L$  configuration when the hopping between the two configurations varies from  $t=0$  to 0.75 eV. The hopping via the  $a_1$  orbital acts effectively as an axial field which pulls down the  $|L_z|=3$  states to lowest energy. **c**, Evolution of the energy levels under the effect of the different contributions to the multiplet Hamiltonian. The diagram starts for the three lowest levels marked by a dashed square in **a**. **d**, Magnification of the energy levels of the ground state octuplet when spin-orbit coupling and Zeeman terms are considered. The zero field splitting is 55 meV. The states shown in red originate from the higher lying quadruplet manifold and they intermix with the ground state octuplet.

## Agreement between multiplet picture and IETS measurements

From the wavefunctions and corresponding energies of the initial state configuration obtained in the multiplet calculations we can calculate the expectation values of any operator that can be written as the sum or product of single electron operators. To simulate the IETS spectrum measured with STM we calculated the spin transition amplitudes using the following expression(30,58) ,

$$I_{i \rightarrow f} = \frac{1}{2} |\langle f | \hat{S}_+ | i \rangle|^2 + \frac{1}{2} |\langle f | \hat{S}_- | i \rangle|^2 + |\langle f | \hat{S}_z | i \rangle|^2. \quad (2)$$

The transition energies correspond to the energy separation of the different states. The two main transitions shown in Figure S6a are indicated by arrows in Fig. S5d. The strong intensity and position of the main step in the simulated IETS spectrum is in excellent agreement with the experimental dI/dV spectrum. It corresponds to a  $\Delta S_z = +1$  transition from the ground state to the second excited state. The steps move in energy in the presence of a magnetic field. To simulate the double step behavior observed in the experiments we assumed a finite 50% population of the first excited state. This is an ad hoc assumption since the spin pumping mechanism of the first excited state is not part of the multiplet model but agrees well with the spin pumping reported in Fig. 5 of the main manuscript. The result is shown in Figure S6b. The transition from the ground state to the second excited state moves to higher energies when the magnetic field is turned on while the transition from the first excited state to the third excited state ( $\Delta S_z = -1$  transition) decreases in energy. The higher energy step at about 90 meV is also in agreement with the experimental spin-polarized IETS spectra (not shown).

## Mapping the ground state multiplet onto an effective Hamiltonian

The proposed effective Hamiltonian differs from previously used spin Hamiltonians (19,31-33) in so far as we include both spin and orbital moment terms instead of spin-only or J-only terms. Two factors motivate this choice. For transition-metal atoms, compared to rare-earth atoms, the spin-orbit coupling is a much smaller perturbation compared to the crystal field, which renders the total moment J not a good quantum number for the Co. Additionally, the Co lowest states have first order orbital momentum, that is, the orbital moment is comparable in size to the spin, so a spin-only picture is not complete either.

For simplicity, we consider here only states arising from a pure  $d^7$  configuration, noting that the splitting of the lowest energy levels remains qualitatively the same as for the mixed  $d^7 + d^8 l$  configuration. In this approximation, the ground state is an octuplet with  $L_z = \pm 3 \otimes S_z = \pm 1.5, \pm 0.5$ . The two lowest states are a spin doublet corresponding to  $S_z = \pm 3/2, L_z = \pm 3$  (L and S are parallel); the next two states correspond to  $S_z = \pm 1/2, L_z = \pm 3$  (also with  $L \cdot S > 0$ ). Higher states of the octuplet have antiparallel L and S coupling. Transitions between the levels ( $|L_z = -3, S_z = -3/2\rangle$  to  $|-3, -1/2\rangle$ ) explain the IETS reported in the manuscript.

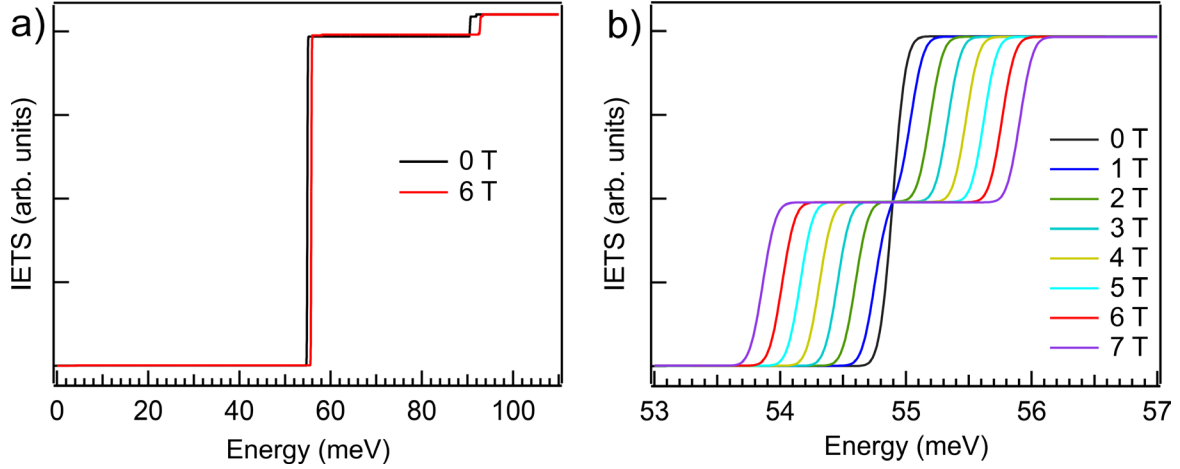


**Figure S6 | IETS spectrum calculated from the  $d^7+d^8l$  multiplet model.** **a**, The simulated IETS spectrum shows two steps in the energy window [0,100] meV with the strongest step at 54.9 meV and a smaller jump at 90.5 meV. The steps move in energy in the presence of an applied out-of-plane magnetic field. **b**, The double step can be simulated assuming a finite population for the first excited state (here equal occupation of ground and first excited state).

This ground state octuplet can be mapped onto an effective Hamiltonian that includes the effect of the crystal field on the orbital moment and spin-orbit coupling in an explicit form:

$$H = H_{CF} + \lambda L \cdot S + \mu_B (L + 2S) B, \quad (3)$$

where  $H_{CF} = B_2^0 L_z^2 + B_4^0 L_z^4 + B_4^4 (L_+^4 + L_-^4)$  is the crystal field Hamiltonian. Only those terms that reflect the four-fold MgO substrate symmetry are included in  $H_{CF}$  (19), where  $B_2^0$ ,  $B_4^0$  and  $B_4^4$  are effective crystal field parameters.

If we use only the leading term of  $H_{CF}$ , with  $B_2^0 < 0$  and sufficiently large to restrict the lowest-lying states to  $L_z = \pm 3$ , this simplified Hamiltonian approximates the multiplet calculation's lowest-energy doublets as  $L_z = \pm 3 \otimes S_z = \pm 3/2$ . Such a modified Hamiltonian describes well the energetics of the system, i.e. it can be used to model the IETS curves of systems (energy splitting) with nonzero first-order orbital moment as is the case here, and to fit the magnetization behavior when Boltzmann statistics applies (at sufficiently high temperatures).

Note that symmetry dictates that the lowest-order nonzero transverse terms in  $H_{CF}$  are  $L_+^4 + L_-^4$ . Neglecting hyperfine coupling effects, these terms cannot mix the lowest states with  $L_z = \pm 3$ . However, to properly describe transition probabilities and associated quantum dynamical processes such as tunneling, the effective Hamiltonian for a single multiplet is not sufficient. Even in a pure  $d^7$  configuration, the lowest energy states are not only pure  $S_z = \pm 3/2$  and  $\pm 1/2$  states, since they contain admixtures of different spins and orbital moments from electronic levels belonging to multiplets higher in energy with respect to the lowest E multiplet (Fig. S5c). This is illustrated schematically in Figure S7.

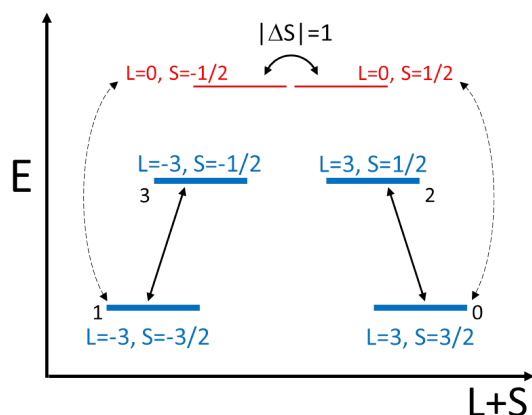


**Figure S7 | Spin-flip transitions and state mixing from the multiplet model.** The energy and magnetic moments of the four lowest states (blue) are well described by the effective Hamiltonian. Allowed spin-flip transitions are indicated by solid arrows. The fourfold crystal field distortion (combined with spin-orbit coupling) leads to small admixture of higher lying states from a different multiplet (red) into the ground state doublet (indicated by dashed arrows) effectively allowing spin-flip transitions between the lowest states.

In the absence of a fourfold distortion spin-flip transitions between the lowest states 0 and 1 are forbidden (as well as between 2 and 3). Only direct vertical transitions between 0,2 and 1,3 have finite probability as indicated by solid arrows in Figure S7. Note that the moment could not reverse by a simple spin-flip process since  $|L|$  would need to change by 6. When the fourfold crystal field distortion is taken into account, the  $B_2$  states, in particular the  $L=0, S=\pm 1/2$  states shown in red in Fig. S7, are mixed into the ground state doublet. Since those states are connected by a  $|\Delta S|=1$  transition, also the new ground state doublet is coupled by a finite spin-flip transition. It is important to note that the mixing of the  $B_2$  state with the E state is a combined effect of both spin-orbit coupling and fourfold crystal field distortion that goes via coupling to higher multiplet states outside the diagram presented in Fig. S5d. Thus the reduction of L and S is traced back to mixing with higher states including  $B_2$  (but not exclusively).

### Upper limit of the zero field splitting

The separation of the first two spin doublets measured by IETS and simulated using the multiplet calculations is  $\sim 60$  meV. For Co on MgO this approximates the full magnitude of the spin-orbit coupling parameter  $\xi$ . This separation is called zero field splitting (ZFS) as it occurs in the absence of a magnetic field. The ZFS represents the energy difference between consecutive states with different orientation of the magnetic moment and defines the barrier for the lowest order process required to reverse the magnetization. The ZFS is therefore a measure of the single-ion magnetic anisotropy energy. A ZFS of the order of  $\xi$  is exceptionally large for a transition-metal atom. It can be shown that  $\xi$  is the maximum energy separation between two consecutive spin-orbit split states that differ by either  $\Delta S_Z=1$  or  $\Delta L_Z = 1$  for a transition-metal. Such a separation is given by the expectation

value of the spin-orbit Hamiltonian  $H_{SOC} = \lambda \mathbf{L} \cdot \mathbf{S}$ , where  $\lambda$  is the atomic spin-orbit coupling parameter ( $\lambda = -\xi/2S$  for the term with largest  $L$  and  $S$  of a configuration with more than five  $d$ -electrons). Since  $|S_z L_z\rangle$  states provide a good approximation to the observed states 1–4, and since  $\langle S_z L_z | \lambda \mathbf{L} \cdot \mathbf{S} | S_z L_z \rangle = \lambda S_z L_z$ , the energy difference for states that differ by  $\Delta S_z = 1$  ( $\Delta L_z = 1$ ) is  $\lambda S_z$  ( $\lambda L_z$ ). For a transition-metal, the maximum energy difference is obtained for a ground state with  $|L_z| = 3$ . This is the case for the ZFS of Co, where  $\lambda L_z = 3\lambda$  which matches  $\xi$ . Note that mixing of states with different  $S_z$ ,  $L_z$  numbers in the ground state due, e.g., to crystal field, would tend to reduce the expectation value of both  $S_z$  and  $L_z$ . Therefore,  $\lambda L_z$  is the upper limit of ZFS induced by spin-orbit coupling.

## References and Notes

1. W. Meiklejohn, Magneto-optics: A thermomagnetic recording technology. *Proc. IEEE* **74**, 1570–1581 (1986). [doi:10.1109/PROC.1986.13669](https://doi.org/10.1109/PROC.1986.13669)
2. P. Carcia, Perpendicular magnetic anisotropy in Pd/Co and Pt/Co thin-film layered structures. *J. Appl. Phys.* **63**, 5066 (1988). [doi:10.1063/1.340404](https://doi.org/10.1063/1.340404)
3. S. Khizroev, D. Litvinov, *Perpendicular Magnetic Recording* (Kluwer Academic Publishers, New York, 2004).
4. S. Monso, B. Rodmacq, S. Auffret, G. Casali, F. Fettar, B. Gilles, B. Dieny, P. Boyer, Crossover from in-plane to perpendicular anisotropy in Pt/CoFe/AlO<sub>x</sub> sandwiches as a function of Al oxidation: A very accurate control of the oxidation of tunnel barriers. *Appl. Phys. Lett.* **80**, 4157 (2002). [doi:10.1063/1.1483122](https://doi.org/10.1063/1.1483122)
5. S. Ikeda, K. Miura, H. Yamamoto, K. Mizunuma, H. D. Gan, M. Endo, S. Kanai, J. Hayakawa, F. Matsukura, H. Ohno, A perpendicular-anisotropy CoFeB-MgO magnetic tunnel junction. *Nat. Mater.* **9**, 721–724 (2010). [doi:10.1038/nmat2804](https://doi.org/10.1038/nmat2804)  
[Medline](#)
6. A. Manchon, C. Ducruet, L. Lombard, S. Auffret, B. Rodmacq, B. Dieny, S. Pizzini, J. Vogel, V. Uhlř, M. Hochstrasser, G. Panaccione, Analysis of oxygen induced anisotropy crossover in Pt/Co/MO<sub>x</sub> trilayers. *J. Appl. Phys.* **104**, 043914 (2008). [doi:10.1063/1.2969711](https://doi.org/10.1063/1.2969711)
7. H. X. Yang, M. Chshiev, B. Dieny, J. H. Lee, A. Manchon, K. H. Shin, First-principles investigation of the very large perpendicular magnetic anisotropy at Fe|MgO and Co|MgO interfaces. *Phys. Rev. B* **84**, 054401 (2011). [doi:10.1103/PhysRevB.84.054401](https://doi.org/10.1103/PhysRevB.84.054401)
8. M. Cubukcu, O. Boule, M. Drouard, K. Garello, C. Onur Avci, I. Mihai Miron, J. Langer, B. Ocker, P. Gambardella, G. Gaudin, Spin-orbit torque magnetization switching of a three-terminal perpendicular magnetic tunnel junction. *Appl. Phys. Lett.* **104**, 042406 (2014). [doi:10.1063/1.4863407](https://doi.org/10.1063/1.4863407)
9. S. Ikeda, H. I. D. E. O. Sato, M. I. C. H. I. H. I. K. O. Yamanouchi, H. U. A. D. O. N. G. Gan, K. A. T. S. U. Y. A. Miura, K. O. T. A. R. O. Mizunuma, S. H. U. N. Kanai, S. H. U. N. S. U. K. E. Fukami, F. U. M. I. H. I. R. O. Matsukura, N. A. O. K. I. Kasai, H. I. D. E. O. Ohno, Recent progress of perpendicular anisotropy magnetic tunnel junctions for nonvolatile VLSI. *SPIN* **02**, 1240003 (2012). [doi:10.1142/S2010324712400036](https://doi.org/10.1142/S2010324712400036)
10. M. Gajek, J. J. Nowak, J. Z. Sun, P. L. Trouilloud, E. J. O'Sullivan, D. W. Abraham, M. C. Gaidis, G. Hu, S. Brown, Y. Zhu, R. P. Robertazzi, W. J. Gallagher, D. C. Worledge, Spin torque switching of 20 nm magnetic tunnel junctions with perpendicular anisotropy. *Appl. Phys. Lett.* **100**, 132408 (2012). [doi:10.1063/1.3694270](https://doi.org/10.1063/1.3694270)
11. J. Z. Sun, Spin-current interaction with a monodomain magnetic body: A model study. *Phys. Rev. B* **62**, 570–578 (2000). [doi:10.1103/PhysRevB.62.570](https://doi.org/10.1103/PhysRevB.62.570)

12. Magnetic anisotropy is often defined as a classical energy barrier, or as the energy needed to orient the magnetization perpendicular to the easy-axis. Our temperature was too low to observe Arrhenius behavior since non-thermal processes dominate the relaxation in the range of temperatures accessed. Additionally studies of quantum magnets sometimes infer a barrier using  $DS^2$  or  $DJ^2$  but these are applicable only for pure-spin or pure-J systems. Consequently, we employ the ZFS as definition of the MA.
13. M. Blume, R. E. Watson, Theory of spin-orbit coupling in atoms. I. Derivation of the spin-orbit coupling constant. *Proc. R. Soc. Lond. A Math. Phys. Sci.* **270**, 127–143 (1962). [doi:10.1098/rspa.1962.0207](https://doi.org/10.1098/rspa.1962.0207)
14. J. van Vleck, *The theory of electric and magnetic susceptibilities* (Oxford Univ. Press, Oxford, 1966).
15. O. Eriksson, B. Johansson, R. C. Albers, A. M. Boring, M. S. S. Brooks, Orbital magnetism in Fe, Co, and Ni. *Phys. Rev. B* **42**, 2707–2710 (1990). [doi:10.1103/PhysRevB.42.2707](https://doi.org/10.1103/PhysRevB.42.2707) [Medline](#)
16. D. Weller, J. Stöhr, R. Nakajima, A. Carl, M. G. Samant, C. Chappert, R. Mégy, P. Beauvillain, P. Veillet, G. A. Held, Microscopic origin of magnetic anisotropy in Au/Co/Au probed with x-ray magnetic circular dichroism. *Phys. Rev. Lett.* **75**, 3752–3755 (1995). [doi:10.1103/PhysRevLett.75.3752](https://doi.org/10.1103/PhysRevLett.75.3752) [Medline](#)
17. P. Gambardella, A. Dallmeyer, K. Maiti, M. C. Malagoli, W. Eberhardt, K. Kern, C. Carbone, Ferromagnetism in one-dimensional monatomic metal chains. *Nature* **416**, 301–304 (2002). [doi:10.1038/416301a](https://doi.org/10.1038/416301a) [Medline](#)
18. P. Gambardella, S. Rusponi, M. Veronese, S. S. Dhesi, C. Grazioli, A. Dallmeyer, I. Cabria, R. Zeller, P. H. Dederichs, K. Kern, C. Carbone, H. Brune, Giant magnetic anisotropy of single cobalt atoms and nanoparticles. *Science* **300**, 1130–1133 (2003). [doi:10.1126/science.1082857](https://doi.org/10.1126/science.1082857) [Medline](#)
19. T. Miyamachi, T. Schuh, T. Märkl, C. Bresch, T. Balashov, A. Stöhr, C. Karlewski, S. André, M. Marthaler, M. Hoffmann, M. Geilhufe, S. Ostanin, W. Hergert, I. Mertig, G. Schön, A. Ernst, W. Wulfhchel, Stabilizing the magnetic moment of single holmium atoms by symmetry. *Nature* **503**, 242–246 (2013). [doi:10.1038/nature12759](https://doi.org/10.1038/nature12759) [Medline](#)
20. A. M. Bryan, W. A. Merrill, W. M. Reiff, J. C. Fettinger, P. P. Power, Synthesis, structural, and magnetic characterization of linear and bent geometry cobalt(II) and nickel(II) amido complexes: evidence of very large spin-orbit coupling effects in rigorously linear coordinated  $\text{Co}^{2+}$ . *Inorg. Chem.* **51**, 3366–3373 (2012). [doi:10.1021/ic2012414](https://doi.org/10.1021/ic2012414) [Medline](#)
21. J. M. Zadrozny, D. J. Xiao, M. Atanasov, G. J. Long, F. Grandjean, F. Neese, J. R. Long, Magnetic blocking in a linear iron(I) complex. *Nat. Chem.* **5**, 577–581 (2013). [doi:10.1038/nchem.1630](https://doi.org/10.1038/nchem.1630) [Medline](#)
22. J. D. Rinehart, J. R. Long, Exploiting single-ion anisotropy in the design of f-element single-molecule magnets. *Chem. Sci.* **2**, 2078 (2011). [doi:10.1039/c1sc00513h](https://doi.org/10.1039/c1sc00513h)

23. J. Klatyk, W. Schnelle, F. R. Wagner, R. Niewa, P. Novák, R. Kniep, M. Waldeck, V. Ksenofontov, P. Gütlich, Large orbital moments and internal magnetic fields in lithium nitridoferrate(I). *Phys. Rev. Lett.* **88**, 207202 (2002).  
[doi:10.1103/PhysRevLett.88.207202](https://doi.org/10.1103/PhysRevLett.88.207202) [Medline](#)
24. A. Jesche, R. W. McCallum, S. Thimmaiah, J. L. Jacobs, V. Taufour, A. Kreyssig, R. S. Houk, S. L. Bud'ko, P. C. Canfield, Giant magnetic anisotropy and tunnelling of the magnetization in  $\text{Li}_2(\text{Li}_{1-x}\text{Fe}_x)\text{N}$ . *Nat. Commun.* **5**, 3333 (2014).  
[doi:10.1038/ncomms4333](https://doi.org/10.1038/ncomms4333) [Medline](#)
25. K. Neyman, C. Inntam, V. Nasluzov, R. Kosarev, N. Rösch, Adsorption of *d*-metal atoms on the regular MgO(001) surface: Density functional study of cluster models embedded in an elastic polarizable environment. *Appl. Phys., A Mater. Sci. Process.* **78**, 823–828 (2004). [doi:10.1007/s00339-003-2437-5](https://doi.org/10.1007/s00339-003-2437-5)
26. Materials and methods are available as supplementary materials on *Science Online*.
27. S. Schintke, S. Messerli, M. Pivetta, F. Patthey, L. Libioulle, M. Stengel, A. De Vita, W. D. Schneider, Insulator at the ultrathin limit: MgO on Ag(001). *Phys. Rev. Lett.* **87**, 276801 (2001). [doi:10.1103/PhysRevLett.87.276801](https://doi.org/10.1103/PhysRevLett.87.276801) [Medline](#)
28. S. Baumann, I. G. Rau, S. Loth, C. P. Lutz, A. J. Heinrich, Measuring the three-dimensional structure of ultrathin insulating films at the atomic scale. *ACS Nano* **8**, 1739–1744 (2014). [doi:10.1021/nn4061034](https://doi.org/10.1021/nn4061034) [Medline](#)
29. A. J. Heinrich, J. A. Gupta, C. P. Lutz, D. M. Eigler, Single-atom spin-flip spectroscopy. *Science* **306**, 466–469 (2004). [doi:10.1126/science.1101077](https://doi.org/10.1126/science.1101077)  
[Medline](#)
30. C. F. Hirjibehedin, C. Y. Lin, A. F. Otte, M. Ternes, C. P. Lutz, B. A. Jones, A. J. Heinrich, Large magnetic anisotropy of a single atomic spin embedded in a surface molecular network. *Science* **317**, 1199–1203 (2007).  
[doi:10.1126/science.1146110](https://doi.org/10.1126/science.1146110) [Medline](#)
31. A. A. Khajetoorians, S. Lounis, B. Chilian, A. T. Costa, L. Zhou, D. L. Mills, J. Wiebe, R. Wiesendanger, Itinerant nature of atom-magnetization excitation by tunneling electrons. *Phys. Rev. Lett.* **106**, 037205 (2011).  
[doi:10.1103/PhysRevLett.106.037205](https://doi.org/10.1103/PhysRevLett.106.037205) [Medline](#)
32. F. Donati, Q. Dubout, G. Autès, F. Patthey, F. Calleja, P. Gambardella, O. V. Yazyev, H. Brune, Magnetic moment and anisotropy of individual Co atoms on graphene. *Phys. Rev. Lett.* **111**, 236801 (2013).  
[doi:10.1103/PhysRevLett.111.236801](https://doi.org/10.1103/PhysRevLett.111.236801) [Medline](#)
33. S. Loth, M. Etzkorn, C. P. Lutz, D. M. Eigler, A. J. Heinrich, Measurement of fast electron spin relaxation times with atomic resolution. *Science* **329**, 1628–1630 (2010). [doi:10.1126/science.1191688](https://doi.org/10.1126/science.1191688) [Medline](#)
34. F. de Groot, High-resolution X-ray emission and X-ray absorption spectroscopy. *Chem. Rev.* **101**, 1779–1808 (2001). [doi:10.1021/cr9900681](https://doi.org/10.1021/cr9900681) [Medline](#)
35. P. Gambardella, S. S. Dhesi, S. Gardonio, C. Grazioli, P. Ohresser, C. Carbone, Localized magnetic states of Fe, Co, and Ni impurities on alkali metal films.

- Phys. Rev. Lett.* **88**, 047202 (2002). [doi:10.1103/PhysRevLett.88.047202](https://doi.org/10.1103/PhysRevLett.88.047202)  
[Medline](#)
36. F. M. F. de Groot, M. Abbate, J. Elp, G. A. Sawatzky, Y. J. Ma, C. T. Chen, F. Sette, Oxygen 1s and cobalt 2p x-ray absorption of cobalt oxides. *J. Phys. Condens. Matter* **5**, 2277–2288 (1993). [doi:10.1088/0953-8984/5/14/023](https://doi.org/10.1088/0953-8984/5/14/023)
37. B. T. Thole, P. Carra, F. Sette, G. van der Laan, X-ray circular dichroism as a probe of orbital magnetization. *Phys. Rev. Lett.* **68**, 1943–1946 (1992).  
[doi:10.1103/PhysRevLett.68.1943](https://doi.org/10.1103/PhysRevLett.68.1943) [Medline](#)
38. P. Carra, B. T. Thole, M. Altarelli, X. Wang, X-ray circular dichroism and local magnetic fields. *Phys. Rev. Lett.* **70**, 694–697 (1993).  
[doi:10.1103/PhysRevLett.70.694](https://doi.org/10.1103/PhysRevLett.70.694) [Medline](#)
39. A. Lehnert, S. Rusponi, M. Etzkorn, S. Ouazi, P. Thakur, H. Brune, Magnetic anisotropy of Fe and Co adatoms and Fe clusters magnetically decoupled from Ni<sub>3</sub>Al(111) by an alumina bilayer. *Phys. Rev. B* **81**, 104430 (2010).  
[doi:10.1103/PhysRevB.81.104430](https://doi.org/10.1103/PhysRevB.81.104430)
40. P.-O. Löwdin, Quantum theory of many-particle systems. I. Physical interpretations by means of density matrices, natural spin-orbitals, and convergence problems in the method of configurational interaction. *Phys. Rev.* **97**, 1474–1489 (1955).  
[doi:10.1103/PhysRev.97.1474](https://doi.org/10.1103/PhysRev.97.1474)
41. B. McGarvey, *Electron spin resonance of transition-metal complexes* Transition Metal Chemistry Vol. 3, R.L. Carlin (Ed.) (Marcel Dekker, 1966).
42. P. Bruno, Tight-binding approach to the orbital magnetic moment and magnetocrystalline anisotropy of transition-metal monolayers. *Phys. Rev. B* **39**, 865–868 (1989). [doi:10.1103/PhysRevB.39.865](https://doi.org/10.1103/PhysRevB.39.865) [Medline](#)
43. J.-P. Gauyacq, N. Lorente, F. D. Novaes, Excitation of local magnetic moments by tunneling electrons. *Prog. Surf. Sci.* **87**, 63–107 (2012).  
[doi:10.1016/j.progsurf.2012.05.003](https://doi.org/10.1016/j.progsurf.2012.05.003)
44. L. Thomas, F. Lioni, R. Ballou, D. Gatteschi, R. Sessoli, B. Barbara, Macroscopic quantum tunnelling of magnetization in a single crystal of nanomagnets. *Nature* **383**, 145–147 (1996). [doi:10.1038/383145a0](https://doi.org/10.1038/383145a0)
45. D. Gatteschi, R. Sessoli, J. Villain, *Molecular Nanomagnets* (Oxford Univ. Press, Oxford, 2006).
46. R. Wiesendanger, Spin mapping at the nanoscale and atomic scale. *Rev. Mod. Phys.* **81**, 1495–1550 (2009). [doi:10.1103/RevModPhys.81.1495](https://doi.org/10.1103/RevModPhys.81.1495)
47. The quantum mechanical description of the energy levels derived from the multiplet calculation indicates that  $J$  is not a good quantum number. Therefore, we use the Zeeman energy  $(L_Z + 2S_Z) \mu_B B$  instead of a description based on the Landé  $g$ -factor.
48. R. Giraud, W. Wernsdorfer, A. M. Tkachuk, D. Mailly, B. Barbara, Nuclear spin driven quantum relaxation in LiY<sub>0.998</sub>Ho<sub>0.002</sub>F<sub>4</sub>. *Phys. Rev. Lett.* **87**, 057203 (2001). [doi:10.1103/PhysRevLett.87.057203](https://doi.org/10.1103/PhysRevLett.87.057203) [Medline](#)

49. G. Feher, E. A. Gere, Electron spin resonance experiments on donors in silicon. II. electron spin relaxation effects. *Phys. Rev.* **114**, 1245–1256 (1959).  
[doi:10.1103/PhysRev.114.1245](https://doi.org/10.1103/PhysRev.114.1245)
50. P. Giannozzi, S. Baroni, N. Bonini, M. Calandra, R. Car, C. Cavazzoni, D. Ceresoli, G. L. Chiarotti, M. Cococcioni, I. Dabo, A. Dal Corso, S. de Gironcoli, S. Fabris, G. Fratesi, R. Gebauer, U. Gerstmann, C. Gougoussis, A. Kokalj, M. Lazzeri, L. Martin-Samos, N. Marzari, F. Mauri, R. Mazzarello, S. Paolini, A. Pasquarello, L. Paulatto, C. Sbraccia, S. Scandolo, G. Sclauzero, A. P. Seitsonen, A. Smogunov, P. Umari, R. M. Wentzcovitch, QUANTUM ESPRESSO: a modular and open-source software project for quantum simulations of materials. *J. Phys. Condens. Matter* **21**, 395502 (2009). [doi:10.1088/0953-8984/21/39/395502](https://doi.org/10.1088/0953-8984/21/39/395502)  
[Medline](#)
51. P. Blaha, K. Schwarz, G. Madsen, D. Kvasnicka, J. Luitz, WIEN2k: An augmented plane wave+ local orbitals program for calculating crystal properties. *Karlheinz Schwarz, Techn. Universitat Wien, Austria* (2001). ISBN 3-9501031-1-2.
52. M. Sgroi, C. Pisani, M. Busso, Ab initio density functional simulation of structural and electronic properties of MgO ultra-thin adlayers on the (001) Ag surface. *Thin Solid Films* **400**, 64–70 (2001). [doi:10.1016/S0040-6090\(01\)01450-X](https://doi.org/10.1016/S0040-6090(01)01450-X)
53. B. C. Stipe, M. A. Rezaei, W. Ho, Single-molecule vibrational spectroscopy and microscopy. *Science* **280**, 1732–1735 (1998). [doi:10.1126/science.280.5370.1732](https://doi.org/10.1126/science.280.5370.1732)  
[Medline](#)
54. R. C. Jaklevic, J. Lambe, Molecular Vibration Spectra by Electron Tunneling. *Phys. Rev. Lett.* **17**, 1139–1140 (1966). [doi:10.1103/PhysRevLett.17.1139](https://doi.org/10.1103/PhysRevLett.17.1139)
55. C. Piamonteze, U. Flechsig, S. Rusponi, J. Dreiser, J. Heidler, M. Schmidt, R. Wetter, M. Calvi, T. Schmidt, H. Pruchova, J. Krempasky, C. Quitmann, H. Brune, F. Nolting, X-Treme beamline at SLS: X-ray magnetic circular and linear dichroism at high field and low temperature. *J. Synchrotron Radiat.* **19**, 661–674 (2012). [doi:10.1107/S0909049512027847](https://doi.org/10.1107/S0909049512027847) [Medline](#)
56. G. van der Laan, B. T. Thole, Strong magnetic x-ray dichroism in 2p absorption spectra of 3d transition-metal ions. *Phys. Rev. B* **43**, 13401–13411 (1991).  
[doi:10.1103/PhysRevB.43.13401](https://doi.org/10.1103/PhysRevB.43.13401) [Medline](#)
57. O. Gunnarsson, K. Schönhammer, Electron spectroscopies for Ce compounds in the impurity model. *Phys. Rev. B* **28**, 4315–4341 (1986).  
[doi:10.1103/PhysRevB.28.4315](https://doi.org/10.1103/PhysRevB.28.4315)
58. N. Lorente, J.-P. Gauyacq, Efficient spin transitions in inelastic electron tunneling spectroscopy. *Phys. Rev. Lett.* **103**, 176601 (2009).  
[doi:10.1103/PhysRevLett.103.176601](https://doi.org/10.1103/PhysRevLett.103.176601) [Medline](#)

plant was slow to recover after removal of the invader (3). How can the clapper rail population be protected while preventing the remaining invasive hybrid *Spartina* population from recolonizing the bay?

To determine the best management strategy for such a situation, Lampert *et al.* constructed a model that constrains the side effects of hybrid *Spartina* management on the clapper rail. The model combines invader removal with the restoration of the native habitat to replace the beneficial

## “How can the clapper rail population be protected while preventing the remaining invasive hybrid *Spartina* population from recolonizing the bay?”

function of the invader. The time scale of the management program is therefore controlled by the rate of recovery of the native and its ability to replace the habitat lost through invader removal.

Removal of invaders can have various negative impacts on nontarget species and ecosystems (4). Native fruit-eating birds, bats, and mammals can incorporate invasive species in their diets (5), presenting conservation conflicts when removal of the resource has an impact on the native consumers. Removal of an invasive predator can lead to overabundance of prey (2) or increased populations of other damaging predators (6). Such nontarget effects of invader management are commonly recognized (7, 8) but are rarely incorporated into optimal management models and are even more rarely assessed in terms of costs (3).

When management of an invader is in conflict with other conservation goals, there are three main options: to continue to manage the impacts of the invader and accept the collateral damage; abandon the management effort and accept the invader impacts; or seek a compromise management strategy that allows both goals to be attained. Several studies have highlighted the importance of assessing or predicting negative effects of invader removal and have recommended the integration of invasive species management with broader ecosystem goals (4), but

few management plans have successfully resolved these conflicts.

This gap between theory and practice is difficult to bridge for several reasons. The complexity and uncertainty of species interactions makes it hard to predict the potential negative impacts of invader removal (9). Population reduction of the invader is often used as the sole criterion for judging the success of invasive species management, and time and resource constraints often limit follow-up monitoring and restoration efforts (10). Another important barrier to an ecosystem-based management approach is the lack of common valuation systems (currencies) that sum and compare the management costs, damages, and benefits (11).

Lampert *et al.* were able to combine the monetary costs of eradication, restoration, and the damages incurred by invasive hybrid *Spartina* with a constraint on the total amount of clapper rail habitat required to find an optimal management strategy. In other systems, however, it can be difficult to determine the costs of impact, and how reversible those costs are with invader removal (12). The costs of the side effects of management actions can also be difficult to assess and quantify. In these cases, it may be appropriate to use evaluation approaches that do not require conversion of different units of measurement into a single currency (11).

There are often large uncertainties in predicting the responses of managed systems. These uncertainties hinder the accurate identification of conservation conflicts and thus the optimization of solutions. We will never be able to predict all risks of environmental management, but the risks of not acting at all may be more serious. Tools like those constructed by Lampert *et al.* are crucial for reconciling the increasing number of conflicts likely to occur. ■

### REFERENCES

1. M. J. Rinella, B. D. Maxwell, P. K. Fay, T. Weaver, R. L. Sheley, *Ecol. Appl.* **19**, 155 (2009).
2. D. M. Bergstrom *et al.*, *J. Appl. Ecol.* **46**, 73 (2009).
3. A. Lampert, A. Hastings, E. D. Grosholz, S. L. Jardine, J. N. Sanichirico, *Science* **344**, 1028 (2014).
4. E. S. Zavaleta *et al.*, *Trends Ecol. Evol.* **16**, 454 (2001).
5. Y. M. Buckley *et al.*, *J. Appl. Ecol.* **43**, 848 (2006).
6. M. J. Rayner, M. E. Hauber, M. J. Imber, R. K. Stamp, M. N. Clout, *Proc. Natl. Acad. Sci. U.S.A.* **104**, 20862 (2007).
7. S. V. Fowler, Q. Paynter, S. Dodd, R. Groenteman, *J. Appl. Ecol.* **49**, 307 (2012).
8. J. Finn, A. P. N. House, Y. M. Buckley, *J. Appl. Ecol.* **47**, 96 (2010).
9. B. Raymond, J. McInnes, J. M. Dambacher, S. Way, D. M. Bergstrom, *J. Appl. Ecol.* **48**, 181 (2011).
10. A. M. Reid, L. Morin, P. O. Downey, K. French, J. G. Virtue, *Biol. Conserv.* **142**, 2342 (2009).
11. I. Grechi *et al.*, *Agric. Syst.* **125**, 1 (2014).
12. H. Yokomizo, H. P. Possingham, M. B. Thomas, Y. M. Buckley, *Ecol. Appl.* **19**, 376 (2009).

<sup>1</sup>School of Natural Sciences and Trinity Centre for Biodiversity Research, Department of Zoology, Trinity College, University of Dublin, Dublin 2, Ireland. <sup>2</sup>ARC Center of Excellence for Environmental Decisions, School of Biological Sciences, University of Queensland, Queensland 4072, Australia. E-mail: buckley@tcd.ie

### PHYSICS

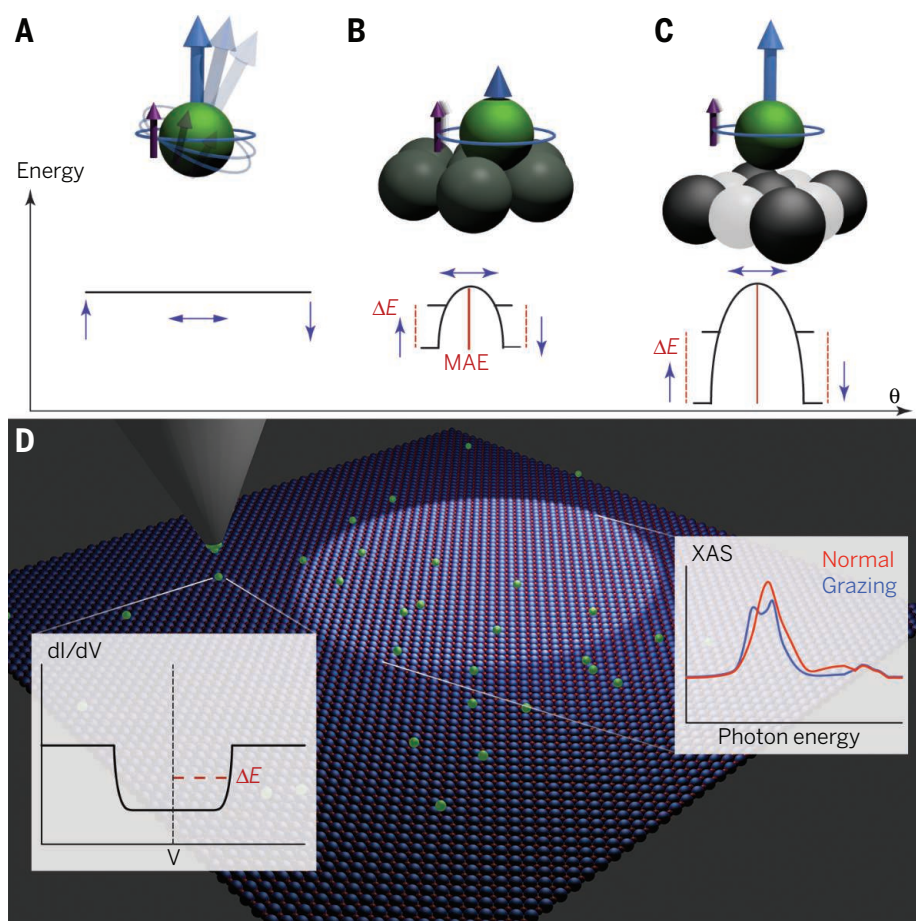
## Hitting the limit of magnetic anisotropy

Enhancing the magnetic properties of adatoms provides a route toward atom-scale memory

By Alexander Ako Khajetoorians  
and Jens Wiebe

Single magnetic atoms adsorbed on surfaces, or so-called adatoms, provide a viable ground for realizing information storage and processing at ultimate length scales (1–3). Such concepts hinge on the magnetic anisotropy energy (MAE), which energetically favors a preferential spatial orientation of the adatom’s magnetic moment  $m$ , where  $m$  is the sum of coupled spin and orbital momenta. Unlike for a free atom, where  $m$  can rotate freely in any direction without energy cost (see the figure, panel A, MAE = 0), large MAE (panel B, MAE  $\neq$  0) enables  $m$  to maintain a fixed orientation for a sufficient amount of time. For stable and robust magnetic memory storage, large values of MAE are desirable. On page 988 of this issue, Rau *et al.* (4) show that a suitable choice of substrate and adatom pairing can result in the further enhancement of MAE, thus providing a possible route toward realizing information storage at the atomic scale.

MAE originates from the so-called ligand field, which is the electrostatic energy generated by the shape of the orbitals of both the adatom and the neighboring substrate atoms, and which breaks the degeneracy of the atomic levels producing the magnetic moment. This energy landscape, combined with spin-orbit coupling (SOC), which locks the spin moment to the orbital moment, generates the resultant MAE. One crucial hurdle toward stabilizing a single adatom is to maximize the MAE, thus protecting  $m$  from thermal fluctuations. Consequently, the three important ingredients for large MAE are a large SOC energy, a large orbital moment, and a strong ligand field. The first condition can be maximized by a proper choice of adatom species. Unfortunately, the



**Atomically controlled magnetism.** Orbital (blue arrow) and spin (purple arrow) moments, and the corresponding MAE for (A) a free Co atom, (B) a Co adatom on a Pt(111) surface, and (C) a Co adatom on an MgO surface. The zero-field splitting energy  $\Delta E$  is a measure of the MAE. (D) Atomic spin detection techniques based on SP-STs and XAS.

other two are usually inversely correlated to each other (i.e., a strong ligand field typically quenches the orbital moment).

In 2003, experiments using x-ray adsorption spectroscopy (XAS) and x-ray magnetic circular dichroism (XMCD) showed that Co adatoms on a platinum(111) metallic surface (see the figure, panel B) exhibited a MAE of 10 meV resulting from strong SOC and an incomplete quenching of the orbital moment (5). With the advancement of single-atom spin detection (see the figure, panel D) based on inelastic scanning tunneling spectroscopy (ISTS) (6, 7) and spin-polarized STS (SP-STs) (8, 9), it was revealed that even in the presence of large MAE, both single Fe and Co adatoms do not exhibit magnetic stability, even at extremely low temperatures. Although the insufficient MAE is one reason for this instability, strong interactions of  $m$  with the underlying metallic substrate electrons further destabilize  $m$  by spin-flip scattering. Therefore, ques-

tions remained whether the MAE could be further enhanced by a choice of substrate that supports a large adatom orbital moment, but at the same time provides a sufficiently strong ligand field, and that limits the coupling of  $m$  to the substrate.

Rau *et al.* show that these challenges can be solved by placing a Co adatom on a thin insulating MgO film (see the figure, panel C). Because of the particular symmetry of the Co adatom on top of an oxygen atom, there is a strong ligand field that keeps particular degeneracies of the Co orbitals. As a result, the orbital moment retains its free atom value and the MAE is pushed toward the SOC limit of the free Co atom of about 60 meV.

Probing the magnetic excitations of the Co adatom with ISTS (see the figure, panel D), Rau *et al.* show that the energy needed to excite the Co adatom is  $\sim 58$  meV. These observations are corroborated by measurements in a magnetic field that confirm the magnetic nature of the excitation. Because ISTS yields little information about the magnetization dynamics of the Co adatom, Rau *et al.* also apply SP-STs based on a pump-probe scheme (7) to probe the relax-

ation time of the excited Co adatom. They find that the time for the magnetic moment to relax to the ground state after excitation over the anisotropy barrier is 0.2 ms, by far the largest lifetime seen for a  $3d$  transition metal atom on any surface. The insulating MgO film evidently decouples the Co moment from interacting with the underlying electron bath.

To gain deeper insight into the orbital configuration that drives the gigantic MAE, and to determine  $m$  of the Co adatom, Rau *et al.* used XAS and XMCD, which are extremely sensitive to the magnetic orientation and orbital configuration of the Co adatom. Such experiments were quantitatively compared to ligand field theory simulations and ab initio calculations, which can precisely determine the multiplet energies of the Co adatom and nicely reproduce the XAS spectra. These results corroborate the STS experiments illustrating that  $m$  strongly favors an out-of-plane orientation with a gigantic MAE. The work of Rau *et al.* presents the first application of all established atomic spin detection techniques, combined with insights from state-of-the-art calculations, to unravel the magnetic properties of an adatom.

Although the MAE reported by Rau *et al.* is record breaking, the observation that the Co adatom still fluctuates on a time scale of hundreds of microseconds certainly places in doubt its feasibility for information storage. Therefore, it is important to ascertain whether such fluctuations are weaker for other adatoms, like Fe, and whether such behavior can be preserved on metallic surfaces. One promising route would be to expand such studies to rare earth metal adatoms or to study whether atomic alloys formed between rare earth and  $3d$  transition metal adatoms can lead to stability. Finally, the viability of single-atom information technology will hinge on the coupling of such single adatoms to arrays that form bits (2, 3) or logic elements (1), and on a minimally disturbing input and readout, leaving room for a bunch of further challenging investigations. ■

#### REFERENCES

1. A. A. Khajetoorians, J. Wiebe, B. Chilian, R. Wiesendanger, *Science* **332**, 1062 (2011).
2. S. Loth, S. Baumann, C. P. Lutz, D. M. Eigler, A. J. Heinrich, *Science* **335**, 196 (2012).
3. A. A. Khajetoorians *et al.*, *Science* **339**, 55 (2013).
4. I. G. Rau *et al.*, *Science* **344**, 988 (2014).
5. P. Gambardella *et al.*, *Science* **300**, 1130 (2003).
6. A. J. Heinrich, J. A. Gupta, C. P. Lutz, D. M. Eigler, *Science* **306**, 466 (2004).
7. S. Loth, M. Etzkorn, C. P. Lutz, D. M. Eigler, A. J. Heinrich, *Science* **329**, 1628 (2010).
8. J. Wiebe, L. Zhou, R. Wiesendanger, *J. Phys. D* **44**, 464009 (2011).
9. A. A. Khajetoorians *et al.*, *Phys. Rev. Lett.* **106**, 037205 (2011).